Master's thesis
Degree Programme in
Materials Research

Experimental Heavy ion Induced X-ray Emission (HIXE) production cross-section with Iodine ion

Ishup Ali Khan

June 2020

Supervisor: Kenichiro Mizohata

Reviewer: Jyrki Räisänen

UNIVERSITY OF HELSINKI
FACULTY OF SCIENCE

HELSINGIN YLIOPISTO
HELSINGFORS UNIVERSITET
UNIVERSITY OF HELSINKI
MATEMAATTIS-LUONNONTIETEELLINEN TIEDEKUNTA
MATEMATISK-NATURVETENSKAPLIGA FAKULTETEN
FACULTY OF SCIENCE

Tiedekunta – Fakultet – Faculty	Koulutusohjelma – Utbildningsprogram – Degree programme	
Faculty of Science	Master's Programme in Materials Research	
Tekijä – Författare – Author		
Ishup Ali Khan		
Työn nimi – Arbetets titel – Title		
Experimental Heavy ion Induced X-ray Emission (HIXE) production cross-section with Iodine ion		
Työn laji – Arbetets art – Level	Aika – Datum – Month and year	Sivumäärä – Sidoantal – Number of pages
Master's Thesis	June 2020	50

Tiivistelmä – Referat – Abstract

Earlier, vast majority of the experiment were performed with PIXE exclusively, with protons as an impinging particle. Due to the concurrence of various phenomena in nuclear and atomic physics like the significant development of the theory of the inner-shell ionization in ion-atom collision, higher sensitivity due to heavy-ions, larger scattering cross-section and larger stopping cross-section HIXE turns out to be a useful technique.

While cross-section of heavy-ion beam at energy few MeV and above have been measured and reported, experimental data for high-energy heavy ions against heavy targets are lack. In this study, X-ray production cross-section induced by iodine ions with energies from 15MeV to 45MeV, produced by 5MV tandem accelerator, have been measured for multiple compounds of thin targets of Ti, Cu, Zn, Ru, Nb, Ta, W and Au in a direct way. Simultaneous measurement of the X-ray data and ERDA data were taken with the help of the x-ray detector and ERDA detector placed at an angle of 120^0 and 30^0 respectively.

Measured cross-section was compared against the ECPSSR and ECPSSR-UA cross-section calculated by the program ISICS11. Experimental cross-section was found above both of the ECPSSR and ECPSSR-UA data.

Thickness of the target from ERDA data were used for the direct calculation of the X-ray production cross-section for 15MeV iodine energy beam.

Additionally, measured cross-section along with the ECPSSR data was compared against the average reduced velocity parameter.

Avainsanat – Nyckelord – Keywords

HIXE, RBS, PWBA, ECPSSR, HI-ERDA, PIXE

Säilytyspaikka – Förvaringställe – Where deposited

Muita tietoja – Övriga uppgifter – Additional information

Experimental Heavy ion Induced X-ray Emission (HIXE) production cross-section with Iodine ion.

Ishup Ali Khan

ABSTRACT

Table of Contents

1 Introduction 6
1.1 Brief history of PIXE method 6
1.2 Heavy ion Induced X-ray Emission (HIXE) 7
2 Purpose of study 8
3 Theory 8
3.1 Characteristic x-rays 8
3.2 Non-characteristic x-rays 9
3.2.1 Atomic bremsstrahlung 10
3.2.2 Secondary electron bremsstrahlung 11
3.2.3 Quasi-free electron bremsstrahlung 12
3.2.4 Nucleus-nucleus bremsstrahlung 13
3.3 HI-ERDA and HIXE 13
3.4 X-ray production Cross section 14
3.5 Theoretical models 15
3.5.1 The PWBA model 15
3.5.2 The ECPSSR model 16
3.6 Determination of cross-section 18
3.7 Sensitivity 19
3.8 Quantitative measurement 19
3.8.1 Counts 19
3.8.2 Target Thickness 20
4 Measurement setup and methods 21
4.1 Accelerator 21
4.1.1 Ion source 23
4.1.2 Acceleration 23
4.1.3 Beam 23
4.1.4 Target 23
4.1.5 Detector and measurement 23
4.1.6 Detector Efficiency 24
4.2 Experimental setup 25
4.3 Analysis and simulation codes 26
5 Results and Discussion 27
5.1 Measurement 27
5.1.1 Peak Area 27
5.1.2 ERDA yields 28
5.1.3 X-ray production cross sections measurements 28
5.1.4 Foil thickness effect 29
5.2 Comparison between theory and experiment 29
5.2.1 Recoil cross-section 29

5.2.2 Comparison against reduced velocity parameters 35
5.2.3 Scattered cross-section 37
6 Conclusion and outlook 38
ACKNOWLEDGEMENTS 39
REFERENCES 40
APPENDICES 43

1 Introduction

1.1 Brief history of PIXE method

Particle Induced X-ray Emission also known as PIXE is an ion beam analysis (IBA) technique. IBA techniques can probe samples non-destructively. The advantage of using IBA methods is that they are non-invasive. They can provide information about the elemental depth distribution, elemental composition and surface properties of the sample. PIXE is an economic, relatively simple, non-destructive and powerful analytical technique and several tens of micrograms (μg) of sample is enough for PIXE experiments(Johansson, 1989). This method can be used to analyze a huge variety of materials, namely pottery and painting, biological tissue, aerosols, wood, water, etc.(Romo-Kröger, 2010) This analysis technique involves exciting the atoms of the specimen with the ion beam of protons, heavy ions or alpha particles and a means of detecting the characteristics X-rays emitted by the target atoms, as they get de-excited. In a typical PIXE spectrum, the area of the characteristic X-ray peaks is related directly to the concentration of the different elements in the specimen.

In the 1950s, accelerators started to be utilized in the nuclear physics research. These accelerators provided a high intense beam of protons or even heavier ions suitable for PIXE analysis. Prior to the use of accelerators, electrons were used as projectiles in early PIXE technique. In 1912, James Chadwick made the first observation of ion-induced X-rays using heavier particles(Chadwick, 1912). Chadwick used α-particles from radioactive sources as projectiles. Alpha particles are emitted during a form of radioactive decay called alpha-decay. They are composite particles consisting of two protons and two neutrons tightly bound together. Later, vast majority of research started using proton as the exciting projectile rather than heavier ions, as they did not show any significant systematic advantage. In addition, ions heavier than helium lead to the deterioration of spectrum quality and possibly damage the sample. The X-ray background hinders emission of X-ray from the cross section of the sample. Due to this lots of research were done to get the information about the role of particle's atomic number and energy in the production of X-rays and the ways to suppress these background X-rays that are augmenting the statistical errors in the X-ray emission spectrum. Theoretically, bremsstrahlung photon intensity for heavy ions are much smaller than for lighter particles such as electrons, due to much smaller deceleration experienced by the ions than for the electrons (Birks *et al.*, 1964). In proton beam the main component of bremsstrahlung was from secondary electrons. Further, capability of simultaneous analysis of many elements, high data accumulation are some advantages of protons over electrons.

Prior to the late 1960s, the main detection option was wavelength-dispersive spectroscopy that could detect only one X-ray line, and therefore one element was analyzed at a time. In the latter part of the 1960s Si (Li) detectors were developed. This stimulated the progress of energy-dispersive spectroscopy using the techniques of multi-channel pulse-height analysis.

In 1970, Johansson *et al.* (T.B. Johansson, R. Akselsson, 1970), at the Lund Institute of Technology first introduced PIXE in a brief exploratory publication. Experimentally,

they showed that it was possible to do multi-elemental analysis at $10^{12}g$ level using protons and Si (Li) spectroscopy.

1.2 Heavy ion Induced X-ray Emission (HIXE)

At the beginning, the vast majority of work used PIXE with protons as an impinging particle almost exclusively. As emphasized by Lapicki (Lapicki, 2005), currently the interest of major researches has shifted to heavy ions. This displacement is due to the concurrence of various phenomena in atomic and nuclear physics like the shifting interest of nuclear physics towards machines with higher energy, greater upturn of knowledge of ion-atom collision physics, and the significant development of the theory of the inner-shell ionization in ion-atom collisions. Additionally, use of other heavy ions based analysis method like Elastic recoil detection analysis (ERDA), MeV-Secondary ion mass spectrometry (SIMS) etc. led to use of PIXE to heavy ions for simultaneous measurement along several techniques.

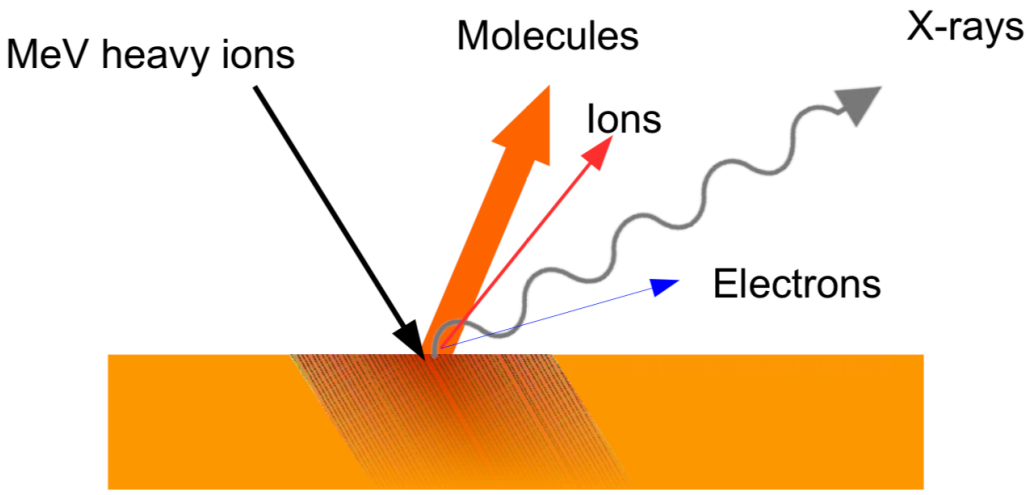

Figure 1: Target impinging of MeV heavy ions((University of Helsinki), 2017)

In Heavy ion Induced X-ray Emission (HIXE) method, instead of using protons as the bombarding particles heavy ions like ^{7}Li, ^{12}C, ^{16}O, ^{28}Si, ^{127}I are used as the projectile. Cross section values for the heavy ions are high in comparison to protons, which means the bigger the mass of the projectile, bigger will be the ionization cross section. In addition, heavy ions are feasible to produce in modern accelerators. High-energy heavy ions can penetrate more deeply in the matter resulting in more precise and detail measurement of the sample.

More promising consideration for the use of heavy ions was, much higher satellites lines were yielded with heavy ions than that of protons with the use of silicon bombardment(Mokuno *et al.*, 1998). As a result of multiple ionization, intense satellite peaks are produced. As the energy spacing of the satellite peaks are too small hence, poor energy resolution, heavy ion bombardment is considered to increase the sensitivity

Thus, ideal analytical conditions can be obtained with the accurate cull of the projectiles with their respective energies and hale perspective of the physical process prompting PIXE and HIXE.

2 Purpose of study

Due to the continual improvement of theoretical models and abundant experimental researches, light ion PIXE (Particle Induced X-ray Emission) has shown great progress over the years. Unlike HIXE (Heavy ion Induced X-ray Emission), a rich database of experimental data can be largely available for the light ion PIXE.
The purpose of this study is to create a standard method to measure X-ray production cross- section using HIXE analysis method. Most importantly, this study produces experimental cross section data, and compares it data from theoretical method. Experimental set up and methods for the analysis are included in the measurement part. Experimental data from the Elastic recoil detection analysis (ERDA) from the lab work was used for the analysis of the X-ray production cross section.

3 Theory

3.1 Characteristic x-rays

When an atom is impinged by ions, which are moving with the velocity higher than the orbital velocity of the electrons in the target atom, the direct Coulomb interaction occurs between the accelerated ions and the electrons in the atomic shell resulting in the ionization. The ionization cross-section depends on the atomic number of the projectile and on its energy, which are essentials for the use of PIXE and HIXE as the multi-elemental analysis method.
As a result, characteristic x-rays are emitted when the electrons thus excited by the ions de-excites. The Coulomb interaction between the bombarding particle forces out the inner shell electrons thus, creating a vacancy in the inner shell. An outer shell electron from higher orbital fills the vacancy. In this transition process, characteristics x-rays are emitted as a result of the energy difference between the shells. Energy levels of each element is different, so these characteristics x-rays help to determine the atom of the element. The binding energy of the electrons in the inner shell is higher than electrons from the outer shell.
Energy of the emitted x-rays is given by:

$$E_e = E_I - E_O \quad (1)$$

Where E_I is the binding energy of the electron in the inner shell and E_O is the binding energy of the electron in the outer shell of the atom.

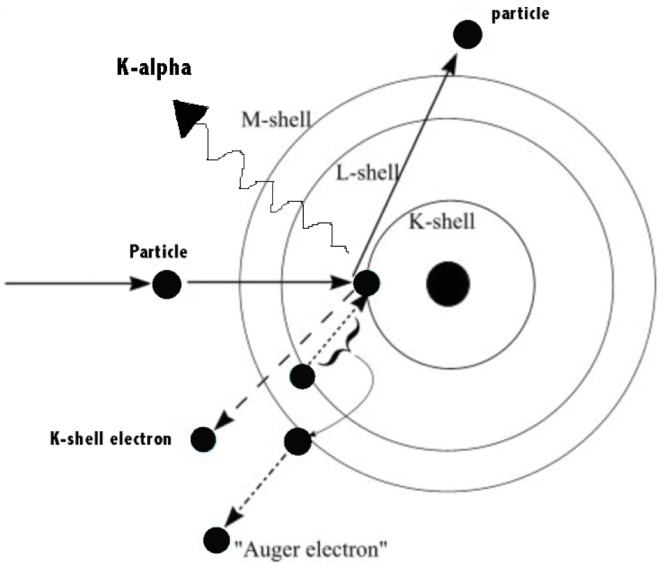

Figure 2: Characteristics x-rays in PIXE method

The x-rays spectra emitted by electrons jumping from higher shells to K-shell to fill the vacancies of atoms are called K-lines as shown in the figure 2. Similarly, spectra emitted when outer shell electrons fall to L-shell is called L-lines and so on. As the energy gap between electron shells of every element is different, therefore K-line for every element are different from one another. X-rays originated from this process are called characteristic x-rays.

The energy of the x-rays can be transferred to one of the outer shell electrons, instead of emitting the redundant energy in the form of x-rays. If this energy is more than the binding energy of the electron, this electron gets ejected from the orbit of the atom. This electron is called Auger electron.

For heavier ions the process of x-rays emission is quite similar, except

In case of heavier ions, depending on their velocity ionization might occurs from an electron promotion mechanism. As the projectile move closer to the target atoms, transient molecular orbitals are formed during the collision. For very close distances of approach of the two nuclei, these quasi-molecular orbitals go over to the orbitals of the quasi-atom corresponding to the sum of the two nuclei. During this process electrons may be promoted from the inner shells to outer shells leaving vacancies after the atoms have receded. The filling of these vacancies by outer shell electrons leads to the emission of characteristic X-rays, either of the target atom or of the projectile.

3.2 Non-characteristic x-rays

When the energetic ions bombard the target, various physical phenomena occur that lead to the production of non-characteristic radiation. This radiation appears in the spectra in the form of continuous backgrounds or enlarged humps. The background in the x-ray spectrum hinders the relevant x-ray counts emitting from the target atom and

increase the chance of statistical errors. In the low energy PIXE method, sources of the background radiation are atomic bremsstrahlung (AB), secondary electron bremsstrahlung (SEB), quasi free-electron bremsstrahlung (QFAB), and nucleus-nucleus bremsstrahlung (NNB).

3.2.1 Atomic bremsstrahlung

During the projectile-target interaction, the target electron is excited to a continuum state, when the electron drops to a lower state it radiates photons with spectra. These spectra are the atomic bremsstrahlung (AB). These spectra are continuum as the emitted photons are drop from different depths in the material losing energy. The energy loss of the photons depends on the depths level of the material and hence the continuum spectrum. These spectra are the dominating spectral range. We can obtain equation for atomic Bremsstrahlung cross-section by using PWBA theory and hydrogen-like wavefunction.(Ishii *et al.*, 2005)

$$\frac{d\sigma^{AB}}{d(\hbar\omega)} = \frac{8a_0^2\alpha^5}{\pi\hbar\omega} Z_p^2 \left(\frac{c}{v_p}\right)^2 \frac{\int_\omega^\infty \frac{dq}{q}}{v_p} \times \left\{1 - \left(\frac{\omega}{qv_p}\right)^2 + \left[\frac{3}{2}\left(\frac{\omega}{qv_p}\right)^2 - \frac{1}{2}\right] sin^2\theta_L\right\} \times \left|Z_p S(Z_T, q)\right|^2 \quad (2)$$

Where $\hbar\omega$ is the energy of the photon, a_0 is the Bohr atomic radius, α is the fine-structure constant, Z_p is projectile's atomic number, Z_T is target's atomic number, c is the speed of light in vacuum, v_p is the velocity of the projectile, θ_L is photon emission angle with respect to the incident projectile direction and $Z_pS(Z_T,q)|^2$ is given in (Ishii and Morita, 1984).

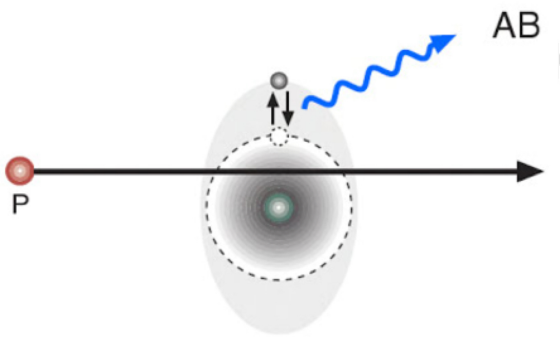

Figure 3: Schematic of atomic bremsstrahlung (1), P is the radiated power along the electron path

3.2.2 Secondary electron bremsstrahlung

The electron in the target atom gets ionized due to the binary collision with the projectile. Electron thus released emits photon upon scattering in the field of a second nearby target nucleus. This process is called Secondary electron bremsstrahlung (SEB). The maximum kinetic energy of the ionized electron determines the maximum photon energy for this process.

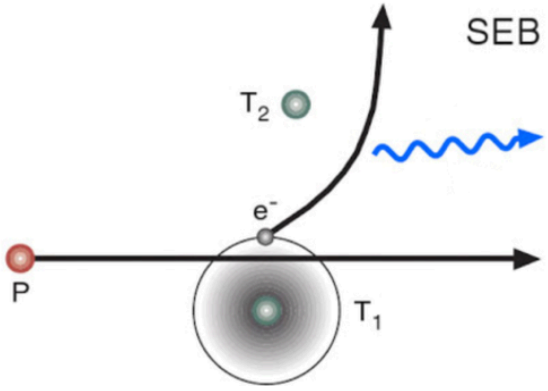

Figure 4: Schematic of Secondary electron bremsstrahlung (1), T_1 and T_2 are the targets

The cross-section of secondary electron bremsstrahlung (SEB) can be obtained by using BEA theory for the electron ejection cross-sections, PWBA equation for electron bremsstrahlung and Bethe equation for the energy loss. (Ishii *et al.*, 2005)

$$\frac{d\sigma^{SEB}}{d(\hbar\omega_L)} = \frac{1}{2\pi} Z_p^2 \left(\frac{e^2}{\hbar c}\right)^5 a_0^2 Z_T \frac{m_e c^2}{(\hbar\omega)^2} (C_1 + C_2 sin^2\theta_L) \quad (3)$$

Where C_1 and C_2 are given in (Yamadera *et al.*, 1981). Secondary electron bremsstrahlung can be characterized by (Murozono *et al.*, 1999) :

$$T_m = 2m_e V_P^2 \quad (4)$$

Where V_P is projectile's velocity and T_m is the maximum energy which the projectile can transfer to a free electron at rest. Above T_m, the intensity of secondary electron bremsstrahlung decreases very quickly. This happens because there are many more free and outer-shell electrons than inner-shell electrons and the bremsstrahlung energy higher than T_m is produced by the target atom's ejected inner-shell electrons.

3.2.3 Quasi-free electron bremsstrahlung

When the velocity of the projectile is much higher than the velocity if the electron in the orbit of the atom, Quasi-free electron bremsstrahlung (QFEB) dominates. This process occurs when the target electron scatters in the Coulomb field of the projectile.

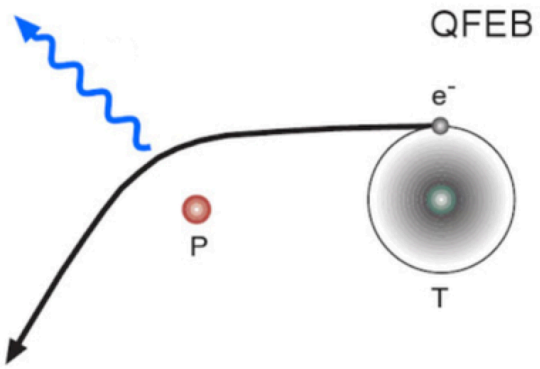

Figure 5: Schematic of QFEB (1)

The equation for the cross section of quasi-free electron bremsstrahlung (Yamadera *et al.*, 1981):

$$\frac{d\sigma^{QFEB}}{d\Omega d(\hbar\omega)} = \frac{N_\tau}{\pi} Z_p^2 \left(\frac{e^2}{\hbar c}\right)^5 a_0^2 \frac{m_e c^2}{T_r \hbar\omega} \times [sin^2\theta + \frac{1}{4}(1+p^2)(3cos^2\theta - 1)\ln\left(\frac{1+p}{1-p}\right) - \frac{1}{2}p(3cos^2\theta - 1)] \quad (5)$$

Where N_τ is the number of electrons of the target atom and $p^2 = 1 - {\hbar\omega}/{T_r}$.

Energy spectrum of QFEB can be characterized by relative kinetic energy T_r (Ishii, 1995):

$$T_r = \frac{m_e E_P}{M_P} \quad (6)$$

Where E_P is energy of the projectile and M_P is mass of the projectile.

3.2.4 Nucleus-nucleus bremsstrahlung

Nucleus-nucleus bremsstrahlung (NNB) results due to the deceleration of the projectile in the field of the target nuclei. Due to this deceleration factor, the intensity is much less for the massive projectile.

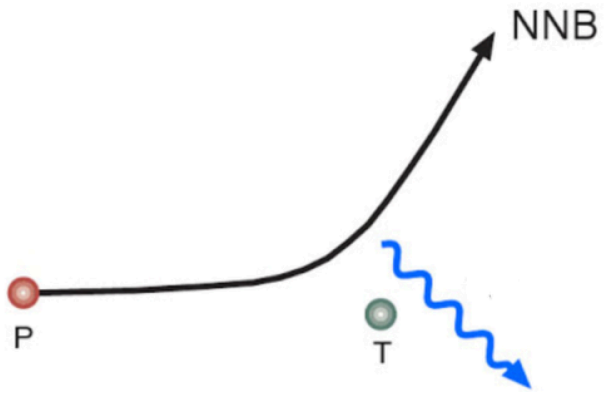

Figure 6: Schematic of NNB (1)

3.3 HI-ERDA and HIXE

Elastic recoil detection analysis (ERDA) is a suitable technique for thin films characterization, determining the elemental depth profiles and sample composition. Heavy Ion elastic recoil detection analysis (HI-ERDA), uses a wide variety of ion beams along with different energies which had led to the significant improvement over traditional ERDA. HI-ERDA equipped with an element or mass sensitive detector is used to identify the recoiled sample atoms and scattered incident ions. In HI-ERDA, all elements present in a sample can be separately detected and analyzed along with their respective depth profiles which can be simultaneously generated from energy spectra using an iterative process. By using various types of Time of Flight (TOF) and gas ionization detector such as Bragg detector and $\Delta E - E$ types detector, different elements can be separated by either their nuclear charge or by their mass. But, the mass separation for heavy elements are quite poor which is one of the limitations of using a low beam energy. This is where the use of HIXE can be beneficial comparatively. Ions of different atoms have different amounts of electric charge, and the more highly charged ones are accelerated most, so the ions separate out according to the amount of charge they have. HIXE can be measured simultaneous with the HI-ERDA. Additionally, HIXE can provide better concentration ratio of heavy components ((University of Helsinki), 2017). Figure 7 shows signals generated by different masses lying on different and discrete curves which makes it easier to identify and analyze each element separately.

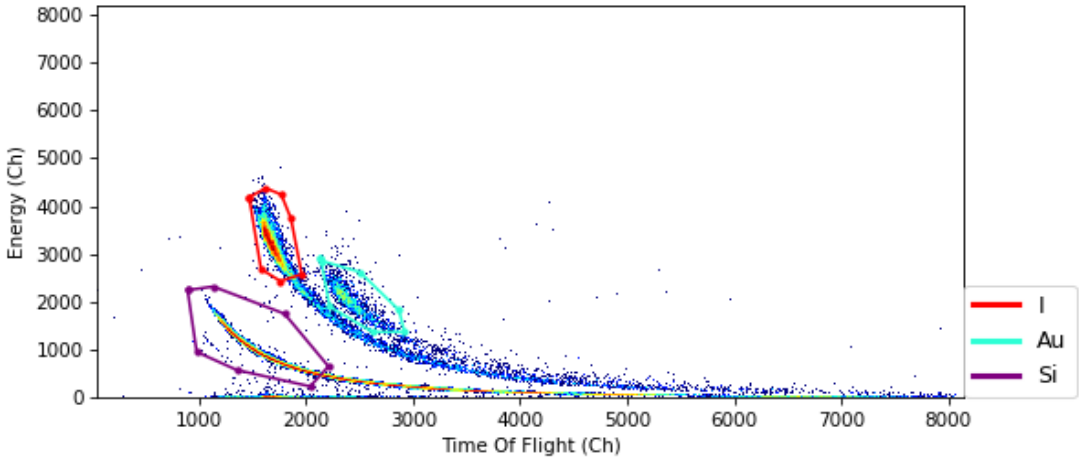

Figure 7: Au on Si using 35MeV $^{126.9}$I beam Time of flight vs energy histogram of the raw data

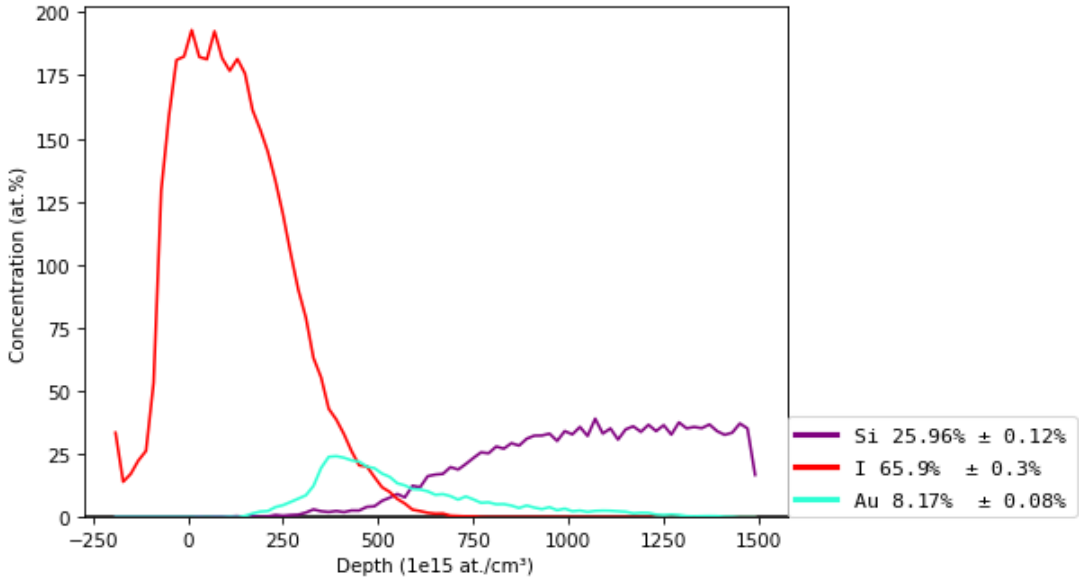

Figure 8: Elemental depth profiles

3.4 X-ray production Cross section

The effective area on the target atom presented to the incident projectile is called the Cross-section. The reaction probability produce in the target atom depends on the cross-section. When the charged particle incident on the target atom, the spectra thus produced due to the ionization depends on the probability cross section to create a vacancy in the definite electronic orbital in the target atom. The ionization cross-section depends on the target atom, the type, charge state and energy of the projectile ion. Energy loss Coulomb-deflection effects; perturbed-stationary-state approximation, with relative correction theories (ECPSRR) is the best theory to calculate the cross-sections for K-shell vacancy produced due to the interaction of the heavy-ion projectile and stationary target atom. ECPSRR theory is based on the Plane-wave Born

approximation (PWBA). Unlike PWBA, ECPSSR also takes into account the Coulomb deflection of the projectile, target atom recoil, increase in the binding of the target K-shell electrons due to the projectile nuclear charge and electron polarization in the target atom (Watson, no date). The main favor for the use of heavy ions in PIXE is the probability of the ionization cross section is higher for bigger projectile ions. Hence, more precise and sensitive results can be obtained from HIXE.

3.5 Theoretical models

PWBA (plane wave born approximation) and ECPSSR (a corrected model of PWBA model incorporating corrective effects) are the two theoretical models used in the experiment for the comparison.

3.5.1 The PWBA model

PWBA is one of the most fundamental approaches utilized in calculations of electron-impact total-ionization cross-sections of atoms. The difference between various calculation methods utilizing the PWBA is mainly in a choice of quality of orbitals used to model the target and residual ion wavefunctions. In this model, the incident ion is described before and after collision by plane wave functions based on the following condition

$$Z_1 v_0 \ll v_1 \leq v_2, \tag{7}$$

where Z_1, v_1 are the atomic number and the velocity of the incident particle, respectively, v_2 the orbital electron velocity and v_0 is the Bohr velocity.

The differential ionization cross-section is given by the equation,

$$\frac{d\sigma}{d\Omega} = \frac{k_f}{k_i} \left(\frac{2\mu}{4\pi\hbar^2}\right)^2 |[\psi_i|V|\psi_f]|^2 \tag{8}$$

where $[\psi_i|V|\psi_f]$ is the transition matrix element, $V_{fi,}$ $|\psi_i]$ and $|\psi_f]$ are the initial and the final wave vectors of the projectile-orbital electron system.

The atomic ionization cross-section is,

$$\sigma_i^{PWBA} = 8\pi a_0^2 \frac{Z_1^2}{Z_{eff}^4 \eta_k} f_K(\eta_K, \vartheta_K), \tag{9}$$

where $Z_{eff} = (Z - c)$ is the effective charge of the atomic shell, c = 0.3 for the K and L_1 shells and c = 4.15 for L_2 and L_3 shells,

$$\eta_K = \frac{m_e E}{M R_h Z_{eff}^2} = \frac{1}{Z_{eff}^2}\left(\frac{e^2}{\hbar v}\right)^2, \tag{10}$$

$$f_K(\eta_K, \vartheta_K) = \int_{W_{min}}^{W_{max}} dw \int_{Q_{min}}^{Q_{max}} |F_W(Q)|^2 \frac{dQ}{Q^2}, \tag{11}$$

with $F(q) = \int \chi_f^*(\vec{r}_2) e^{i\vec{q}.\vec{r}} \chi_i(\vec{r}_2) d\vec{r}_2$, and $\chi_i(\vec{r}_2)$, $\chi_f(\vec{r}_2)$ are non-relativistic wave functions of atomic electrons and $\chi_i^*(\vec{r}_2) et \chi_f^*(\vec{r}_2)$ are the complex conjugates of the wave functions, $Q = (a_s, q_s)^2$, a_s and q_s are the radius of the atomic shell and the transferred momentum relative to the atom shell s, respectively (Hansteen *et al.*, 2017).

3.5.2 The ECPSSR model

The ECPSSR model was proposed by Brandt and Lapicki (Lapicki *et al.*, 1981). They modified the PWBA model by incorporating polarization and binding effects in the PSS (perturbed stationary state approximation) and including relativistic (R), energy loss (E), and coulomb deflection (C) effects in it and referred as the ECPSSR theory (Lapicki and Losonsky, 1979). It reduced the disagreement between experiment and theory but only for the K shell and for light projectiles. In the case of L-shell ionization, the deviations from the theory have been observed in the low ion velocity range. When the collision energy decreases the discrepancy between these simple theories and experiments becomes significant and modifications should be made. Further, at lower energies, a refinement has been made in ECPSSR theory which is entitled as "united atom" approximation (UA). The ionization cross-section is given by,

$$\sigma^{ECPSSR} = C_s\left(dq_{0_s}\right) F_s(Z) \sigma^{PWBA}(m^R(\xi_s)\eta_s, \zeta_s \vartheta_s), \tag{12}$$

where $C_s\left(dq_{0_s}\right)$ is the coulombian deflection term, $F_s(Z)$ is the energy loss correction factor(Brandt and Lapicki, 1981), $m^R(\xi_s)\eta_s$ and $\zeta_s \vartheta_s$ represents the relativistic and the binding energy corrections(Brandt and Lapicki, 1979b), respectively, where

$$\zeta_s = 1 + \left(\frac{2Z_1}{Z_s \vartheta_s}\right)(G_s - H_s) \tag{13}$$

is the binding energy correction factor and,

$$m^R(\xi_s) \cong \sqrt{(1 + \beta Y_s^2)} + Y_s$$

(14)

is the relativistic mass(Lapicki, Laubert and Brandt, 1980).
Hence, the X-ray production cross-section for K-shell is written as

$$\sigma_x = \sigma_i \omega, \tag{15}$$

where ω is the fluorescence yield factor.

Since the early 1970s the ionization of K-, L- and M-shell electrons by heavy charged particles has been intensively studied in asymmetric collisions where the projectile is lighter than the target ($Z_1 \ll Z_2$). All of these studies have led to the satisfactory understanding of fundamental process, particularly for light projectiles and K-shell using basic approaches and principles of PWBA and semi-classical approximation (SCA). Due to much stronger perturbation of target electrons by the increased Coulomb field of the projectile following phenomena have to be considered.

3.5.2.1 ECPSSR-UA

Basic ECPSSR theory modified the PWBA model and reduced the disagreement between the theory and experiment. But the agreement holds only for the K-shell and for light projectiles and starts to deviate for L-shell ionization in the low projectile velocity range. Significant discrepancy between these simple theories were seen as the velocity of the projectile decreases. ECPSSR-UA (ECPSSR-United Atom approximation) is a refinement done to overcome this discrepancy at low energies which corrects the unphysical behaviour of atomic level binding energy in ECPSSR theory using the procedure suggested by (Cipolla, 2007) and termed it as ECPSSRUA which implies the UA effect increases rapidly with the decrease in the proton energy. But this refinement also gave erratic results when the experimental data were compared with the theoretical predictions.

3.5.2.2 ECPSSR-MI

During the collisions of atoms with ions, simultaneous ejection of several electrons occurs due to the strong Coulomb field of the projectile. This effect is called as the multiple ionization (Manpuneet Kaur, Harsh Mohan, Arvind K. Jain, Parjit S. Singh, 2017). The collision process leads to the creation of multiple vacancies in the outer shells. These vacancies act as spectators and may not filled prior to the radiative filling of inner-shell vacancy. As a result, reduction of the screening of nuclear charge takes place which give rise to increase of the binding energy of all energy levels. Thereupon, both width and position of the emitted x-rays from multiple ionized atoms gets shifted considerably. This effect also ensues in the increase of Fluorescence yields which decreases as the velocity of the projectile goes down. Multiple ionization of incoming ions strongly affects the factors required for the extraction of cross-section namely Fluorescence and Coster-Kronig yields. Hence, multiple ionization effect has been

included in the ECPSSR theory so as to meet the necessity to refine and improve the cross-section calculation. One way to decrease the probability of multiple ionization is to increase the target atomic number as binding energies of the outer-shell electrons increases with the increasing atomic number.

3.5.2.3 ECPSSR-IS

Several anomalies were found in the L-shell ionization using heavy projectile ions. Large deviation was found between the measured cross-section values and the predictions of the first-order ionization theories. An idea of the vacancy rearrangement (Mukoyama and Sarkadi, 1981) was introduced as an attempt to account for all these discrepancies. Accordingly, this idea implies that at relatively small velocity of the projectile with heavy ion target a redistribution of the vacancies may take place between the subshells. In other word, the vacancy produced by the direct ionization in one of the L subshells may transfer to another subshell with a considerable probability as a result of a secondary interaction between the projectile and the target electrons. Possible interference effects were neglected during the coupling between the L-substates, as they were described by transition probabilities instead of transition amplitude. Hence, more refined approaches were worked out based on second order Born approximation and the coupled channel formalism in ECPSSR- Intra-subshell coupling (ECPSSR-IS).

3.6 Determination of cross-section

The cross-section measurements were performed for the elements Au, W, Ti, Ta, Zn, Ru, Nb and Cu. Iodine with 15MeV, 30MeV, 35MeV, 40MeV and 45MeV energies were used as incident beam. In this experiment the X-ray production cross section was determined using two different formulae. One with the target thickness and the other independent of the target thickness and beam fluence normalized to ERDA. For 15MeV beam energy and some elements under 35MeV beam energy, the X-ray production cross-section was determined by the formula using the target thickness and is given by

$$\sigma_X = \frac{Y_X}{\epsilon n N_X} \tag{16}$$

where σ_X is the X-ray production cross-section, Y_X = (l_α+ l_β) or (k_α+ k_β) is the sum of the measured x-ray yields for l-alpha and l-beta or k-alpha and k-beta depending on the elements. ϵ is the efficiency of the detector, which was taken as 1. $n = \frac{Q}{q_e}$ is the number of electrons, Q is total charge and q_e is charge on each electron. N_X is the target thickness calculated from ERDA data.

For rest of the beam energy, the X-ray production cross-section was determined using the formula

$$\sigma_X(E_1) = \left(\frac{Y_{X\alpha} + Y_{X\beta}}{\epsilon}\right) \Omega_{ERD} \frac{\frac{d\sigma}{d\Omega}(E_1)}{Y_S(E_1)}$$

(17)

where $Y_{X\alpha}, Y_{X\beta}$ are the measured l-alpha, l-beta or k-alpha, k-beta x-ray yields, $\Omega_{ERD} = 0.19 * 10^{-3} str$ is the charged particle solid angle, Y_S is the measured recoil or scattering yield at laboratory angle 40°, $\frac{d\sigma}{d\Omega}$ is the Rutherford differential cross-section at beam energy E_1. The Rutherford differential cross-section for recoils was given by the formula

$$\frac{d\sigma}{d\Omega} = \left(\frac{Z_1 Z_2 \hbar c \alpha (m_1 + m_2)}{2E_1 m_1}\right)^2 \frac{1}{cos^3\theta} \tag{18}$$

where Z_1, Z_2 are the atomic number, m_1, m_2 are the atomic mass of the elements, E_1 is the beam energy, θ is the scattering angle, $\alpha \approx \frac{1}{137}$ is the dimensionless fine structure constant, $\hbar c \approx 197\ MeV.fm$. The Rutherford differential cross-section for scatterings was given by the formula

$$\frac{d\sigma}{d\Omega} = \left(\frac{Z_1 Z_2 \alpha (\hbar c)}{4E_1 sin^2\, \theta/_2}\right)^2 \tag{19}$$

In case, where the beam is much heavier than the target for example I on Cu, beam is not scattered to an angle of 40°. The maximum angle for scattered beam in ERDA, is called critical angle and it is equal to $\theta\ \max = \text{asin}\ (m2/m1)$. So, equation (19), gives the differential cross-section for the scattered beam for the elements heavier than the beam.

3.7 Sensitivity

PIXE and HIXE both have high sensitivities for the analysis of trace elements. Other matrix effects like particle stopping power, or particle energy loss per unit distance of penetration in the sample are some factors that affect the sensitivity of these analyses. Both characteristic and non-characteristic radiation from the background generation influence the sensitivity of the analysis. If the electron binding energy of the target atom is below the incident projectile, a high sensitivity will be obtained.

3.8 Quantitative measurement

3.8.1 Counts

Concentration of the element in the sample can be obtained from PIXE spectra using the formula(Johansson, 1989):

$$dN = A(s)n(s)\sigma\omega k\Omega T\ \varepsilon dS \tag{21}$$

Where dN is the number of counts from the number of atoms A(s). n(s) is the number of protons going through the surface element dS. σ and ω are the cross section for ionization and the fluorescent yield respectively, k is the probability for relative transition for the x-ray transition used in experiments. Ω is the solid angle. ε is detector's efficiency. T is transmission through irradiation chamber window. It also includes absorption by absorber, if one is used, and sample's self-absorption.

Integrating the (7) gives the total number of counts N in specific peak. If the beam density distribution is uniform, n(s) is taken to be constant. So, by integrating A(s) over the whole surface, total number of counts is:

$$N = An\sigma\omega k\Omega t\varepsilon \tag{22}$$

Where A is the total number of atoms of an element in a sample. Experimentally, by fitting certain polynomial background model to spectrum and Gaussian to each peak the values of N for each peak can be obtained by using software.

The composition of inhomogeneous sample can be known with the help of standard sample of known composition by irradiating them both in similar conditions and normalizing the sample's peak areas with the peak areas of the standard sample.

3.8.2 Target Thickness

If the scattering angle θ and the solid angle Ω are well defined by the instruments and the σ scattering cross-section can be calculated using equation (18) or (19), the number of target atoms per unit area is given by

$$A = \sigma\Omega QNt \tag{23}$$

where Q is the total number of incident particles, A is the number of detected particles Nt is the number of target atoms per unit area. Table 1(a) and 1(b) below shows some of the target thickness obtained experimentally for different samples.

Table: 1(a) Own samples

	TiO_2	CuO	Ta_2O_5	WN_x
	1E 15at/cm^2	1E 15at/cm^2	1E 15at/cm^2	1E 15at/cm^2
Metal	341.2	213.4	409.1	137.7
O	684.7	211	1129.5	69.3
N				145.5
C	6.9	0.8	22.3	43.6
H	18.6	5.6	63.5	47.6

((University of Helsinki), 2017)

Table: 1(b) CRP shared samples, ~20nm

	TiN	ZnO	NbO_2	RuO_2	Ta_2O_5
	1E 15at/cm^2	1E 15at/cm^2	1E 15at/cm^2	1E 15at/cm^2	1E 15at/cm^2
Metal	138	217	88	67	50.6
O	16.7	225	232	76	150.3
N	144				
H	4.4	2.3	76	3.7	48

((University of Helsinki), 2017)

4 Measurement setup and methods

4.1 Accelerator

In the laboratory, PIXE experiments are carried out with 5MV tandem accelerator in the beam line 3. There is also 500 kV KIIA ion implanter in the laboratory. A layout of the main accelerators in the laboratory is shown in the figure 9. All the main components of the accelerator system related to the PIXE and HIXE measurements, from the ion source to the beam line is shown in the figure 7.

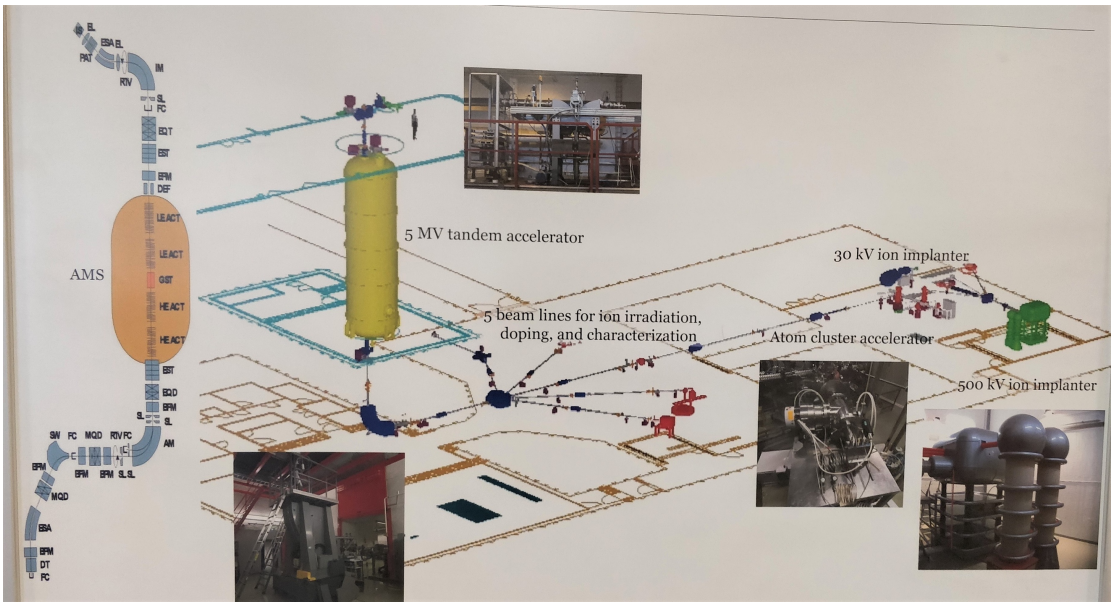

Figure 9: layout of the main accelerator laboratory

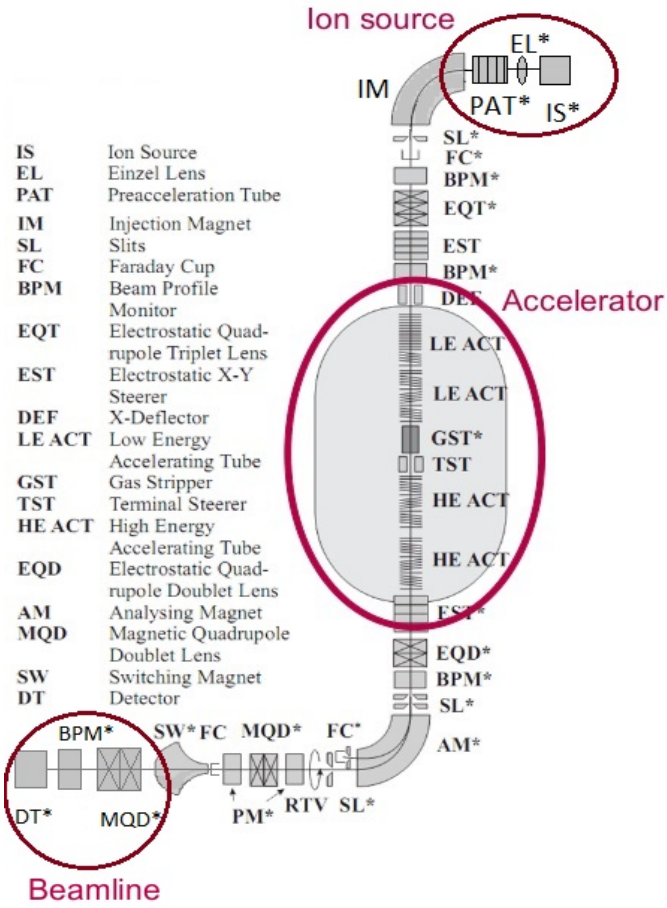

Figure 10: Overview of all parts in the beam path (*Accelerator Laboratory | Faculty of Science | University of Helsinki*)

4.1.1 Ion source

Cesium vapor is injected from the cesium oven into an enclosed area between the cooled cathode connected to the negative high voltage potential and hot ionizing surface. Some of the Cs gets ionized by the ionizing surface and some gets condensed on the front of the cathode. Ionized cesium accelerates towards the cathode and is focused on the front face of the cathode causing sputtering of particles. These particles go through the condensed cesium layers. Hence, negative ions are accelerated from the cathode surface.(*Ion Beam Sources Archives - National Electrostatics Corp.*)

4.1.2 Acceleration

Injection magnet directs the negative ions produced from the ion source to the accelerator. TAMIA 5MV tandem Van De Graaff- accelerator EGP-10-II was used for the irradiation experiments. The accelerator uses two stage tandem acceleration and Van De Graaff generator to get desired energy ions. A few kilovolt dc power supply is connected to a brush of metal wires in the Van De Graaff generator. The conveyor belt carries the corona discharge generated between the belt and wires to the high voltage terminal. The negative ions from the ion source gets accelerated when they move towards the positive high voltage terminal, this process occurs in tandem accelerator. The second stage of acceleration begins when electrons from the negative ions are stripped off, repelling the positive proton beam by the positive high voltage terminal, this process occurs in gas stripping canal(Gove, 1969). The accelerator used for the measurement is located in accelerator laboratory of the University of Helsinki's faculty of science, division of material physics Kumpula, Helsinki.

4.1.3 Beam

Beam Profile Monitor (BPM), measures the beam current and analyzing magnets led the beam to the beam line. These experiments were carried out in vacuum and the beam line was TOF-ERDA beam line. 15MeV-45MeV $^{126.9}$I beam was provided for the experiments from the accelerator.

4.1.4 Target

Targets used in the experiments includes elemental and compounds of Ti, Zn, Nb, Ru, Ta, oxides and nitrides on C or Si. Other targets like Cu, Ta, W, Au Atomic layer deposition (ALD) deposited oxides, nitrides and elemental targets on Si were also used.

4.1.5 Detector and measurement

Canberra Ultra LEGe detector GUL0110, detector with the performance range from few hundred electron volts to a few hundred kilo electron volts is used in this experiment. It has an area of 100mm^2 and thickness of 10mm with the resolution of less than 150eV at 5,9keV. 0.03mm Beryllium window was used as a detector window.

Measurements were done with 950V reverse bias where an electric field extent across depleted region in P-I-N structured Germanium detector. When the x-ray from the sample interact with the depleted material of the detector, charge carriers are produced which are swept to electrodes under electric field. Energy received from the radiation is proportional to these charges.

Canberra I-TRP model preamplifier converts the collected charge to voltage. This preamplifier, also called "Integrated Transistor Reset Preamplifier" eliminates long recovery time caused by illumination of FET and is suitable for applications with high count rate. Coaxial cables connect the preamplifier to the Canberra model 2026 amplifier and Canberra high voltage power supply model 3106D. Linear amplifier is connected to Dual ADC model 7072 analog-to-digital converter, which is then connected to the multi-channel analyzer (MCA) and to the computer. Spectrum size was adjusted to 2048 channels in ADC and Gaussian pulse shaping with shaping time of 12 μs was used with a coarse gain of 100.

Due to the low band gap of germanium, noise occurs caused by the thermal generation of charge carriers. In order to reduce the noise, detector was cooled with liquid nitrogen (LN_2). A dewar vessel was filled 8 hours prior to the measurement to match with the cooling time. Measurements can be carried out for 2-3 days before the dewar had to be refilled.

Absorbers like aluminum and mylar can be used to distinguish desired elements in a spectrum. These absorbers absorb low-energy bremsstrahlung x-rays from the secondary electrons. Funny filters can be used to avoid excess absorption of the characteristics x-rays from the light elements. These filters are absorbers with tiny hole at the center, the size of the hole is usually a few percent of the detector surface area (Nejedly, Campbell and Gama, 2004). Funny filters greatly reduce the intensity of the high cross-section x-rays from light elements and has zero effect on the less intense high energy x-rays. Absorber material of the filter absorbs light element x-rays and rest pass through the hole in the middle. (Roumié *et al.*, 2005).
In the experiment, a 12.5μm Cr funny filter absorber was used in the experimental setup. It was placed in front of the detector window between the detector and the sample to reduce the effect of iron and light element x-rays in the PIXE spectrum.

4.1.6 Detector Efficiency

The Ultra-LEGe retains the high-energy efficiency intrinsic to germanium detectors because of the high atomic number (Z) and thus covers a wider range of energies than any single-photon detector.

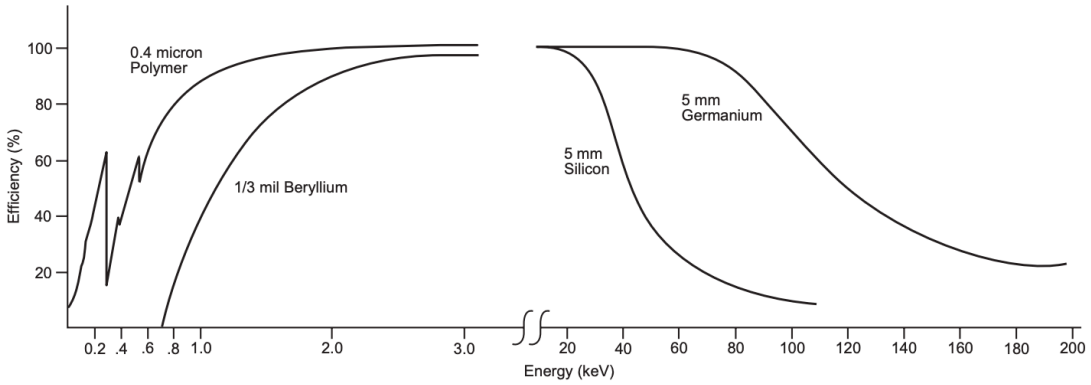

Figure 11: Comparison of window transmission-Polymer vs Beryllium(*Ultra-LEGe Detector Features*)

For the experiment, the detector was calibrated using ^{55}Fe x-ray source and proton PIXE yield. The detector efficiency (ϵ) was taken as 1 for the experiment.

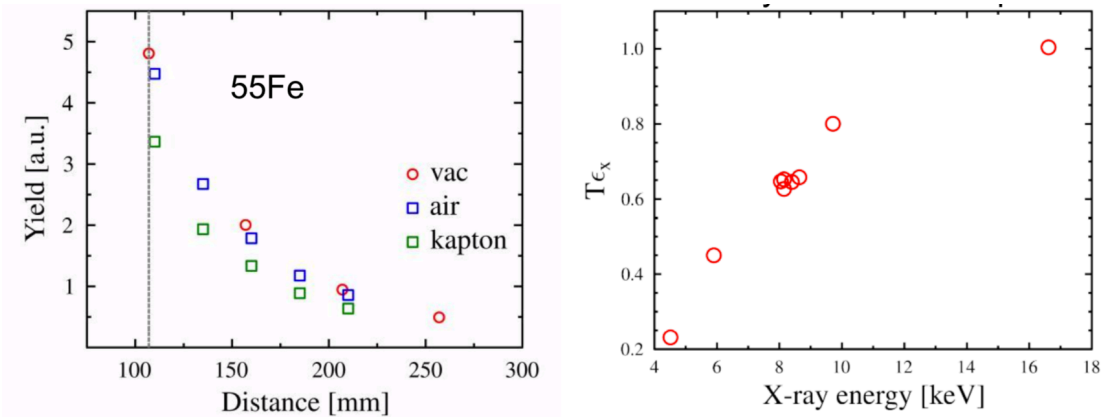

(a) (b)

Figure 12: (a) Distance to Yield, (b) PIXE efficiency and window absorption((University of Helsinki), 2017)

4.2 Experimental setup

Figure 13 and figure 14 shows the experimental arrangements. The setup for the TOF-ERDA in the University of Helsinki consists of an ion implanted energy detector and

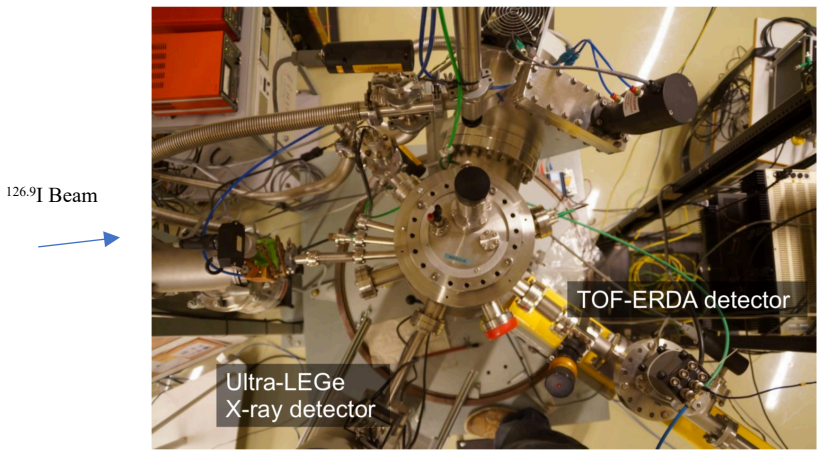

Figure 13: Experimental arrangement (University of Helsinki), 2017)

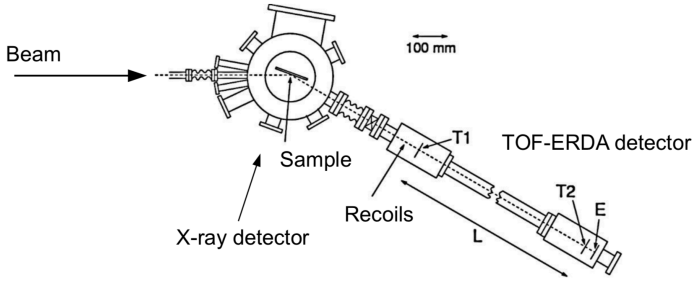

Figure 14: Schema of the ToF telescope detector.((University of Helsinki), 2017)

two-timing gates. Figure 14 shows the detail schema of the measurement system. A thin diamond like carbon (DLC) film was fitted into the timing gates with the thickness ranging from 3.1 µg/cm2 and 9.0 µg/cm2 in the first and second gates, respectively. As the ions passes through the films, secondary electrons are emitted which gets multiplied at micro-channel-plates (MCP). These electrons are accelerated and directed to MCP with an electrostatic field. The anode signal generated by the collection of these electrons at anode is directed to a constant fraction discriminator. The signals from the timing gates were then directed to a time-to-digital converter. As the energy and depth resolution are important factors in the analysis of very thin samples, using thin DLC foils in the timing gates reduced the effect of straggling and multiple scattering to the energy resolution. Hence, comparing with the carbon foils, the timing and homogeneity was better controlled for DLC films(Mizohata, 2012).
The equipment used for ERDA techniques fitted with special detectors allow the separation of different recoil species separated either by their mass or nuclear charge. This separation can be achieved by using different TOF and gas ionization detectors such as Bragg detector and various types of ΔE–E detectors. The detector angle was determined to be 40.0 ± 0.1◦ by comparing the yields of scattered and recoiled ions from thin sample films. Typically, the measurements were taken geometrically whereby both the incident and exit angles where equal to 20º to the sample surface. X-ray detector was placed at an angle of 120º, 10º normal from the sample.

4.3 Analysis and simulation codes

The data obtained from the experiment were normalized and computed using R. Additionally, the channels from the data were converted to respective energy using R for plotting. Origin pro software was used for the plotting and further peak fitting of the graphs as well as plotting for the cross-section. All individual peaks were fitted, and area covered under the peaks were calculated using integration. POTKU software was used to calculate the scattering or recoil yields from the ERDA data. Finally, DOSBOX was used as an emulator to run the ISICS code to calculate the theoretical cross-section to be compared with the experimental x-ray production cross-section.

5 Results and Discussion

5.1 Measurement

5.1.1 Peak Area

Peaks obtained from the x-ray data were fitted and plotted using origin pro. Area for the individual peaks were calculated using integration and individual alpha and beta peaks were summed according to the target elements. Area of K-alpha and K-beta peaks were obtained for the lighter elements, whereas L-alpha and L-beta peaks were obtained for the heavier elements. Some background peaks were also obtained during the experiments. The Kα intensity for Nb and Ru were measured only at highest energy as the lower cross-section makes the background subtraction on the Kβ line more critical. Figure 15 shows the energy to counts plot for the 40MeV $^{126.9}$I beam on WN sample. In the figure 15, the L-alpha and L-beta peaks of the Tungsten(W), were formed at approximately 8keV and 9keV respectively, which was in the range of theoretical values 8.398keV and 9.672keV. Area of the overlapped peaks were combined to get the total area. Error in the area was calculate as the square root of the calculated area.

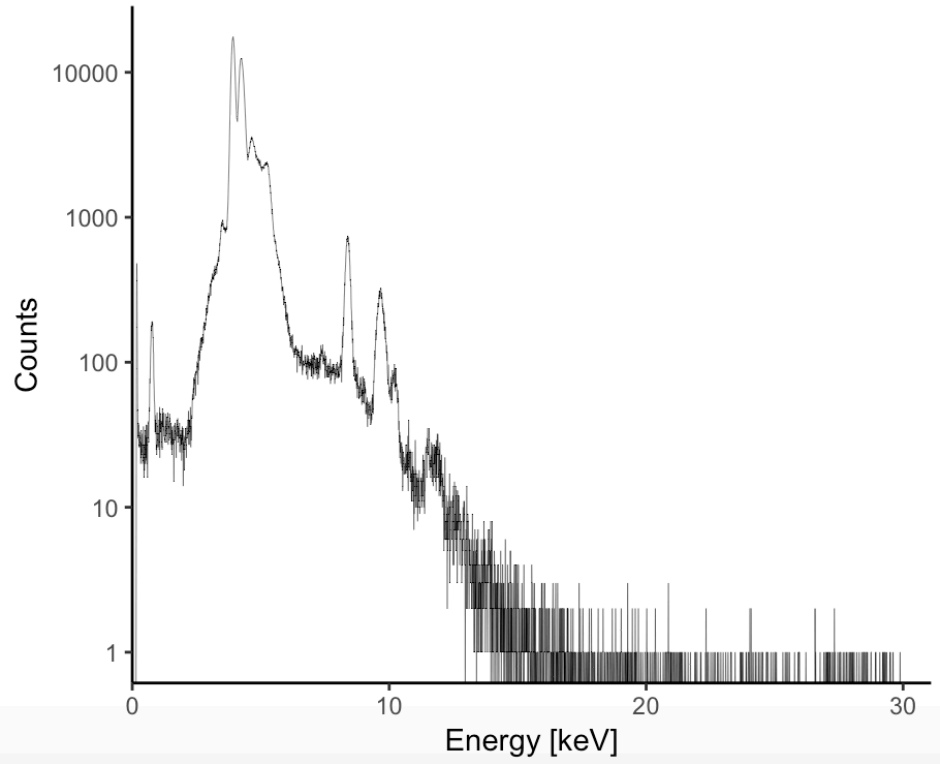

Figure 15: Peaks for 40MeV $^{126.9}$I on WN

Due to peak energy shifts and broadening, the Lα line of W has been integrated at all energies and similar procedure for the other L lines along with a complete fitting of the corresponding energy regions. A global statistical error of about ±5% for Ti, Cu, Zn, Ta, W, Au and of about ±10% for Nb and Ru for cross-section was estimated.

5.1.2 ERDA yields

Along with the x-ray data, ERDA were also calculated simultaneously. The collected raw ERDA data were analyzed using POTKU software. Settings were configured according to the charge state, detector angle, and beam energy.

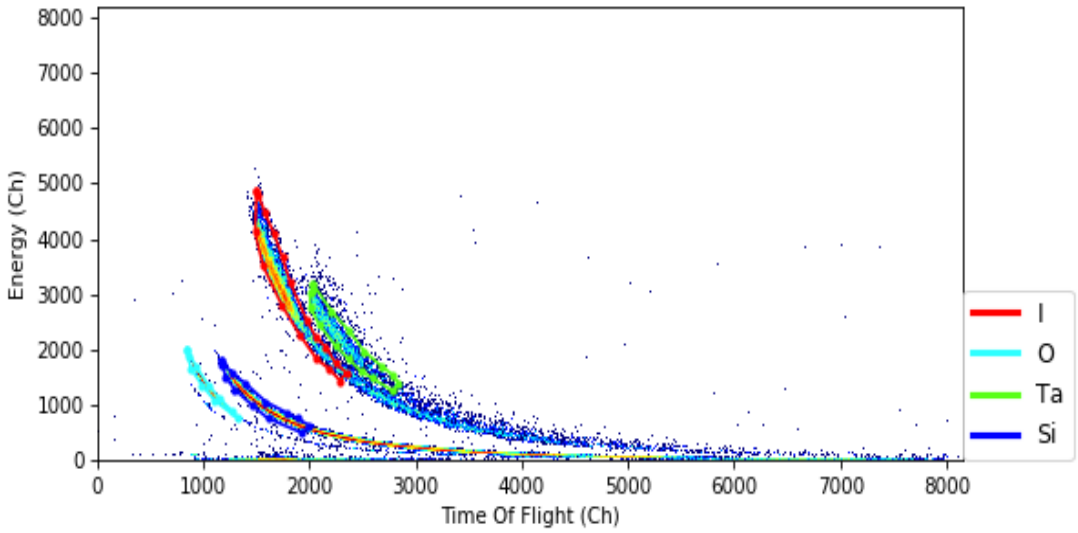

Figure 16: Cuts for 40MeV $^{126.9}I_{7+}$ on Ta_2O_5

Figure 16 shows the cuts for individual elements during the bombardment of 40MeV iodine beam on the Ta_2O_5 sample. All of these cuts were saved, and individual cuts were analyzed and recorded to be used as recoil or scattering yields depending on the element is heavy or light respectively. Ta recoils were calculated using equation 18 from the analyzed cut data for the figure 16.

5.1.3 X-ray production cross sections measurements

The measured x-ray yields from peak area and ERDA yields were used to calculate the x-ray production cross-section using equation 17. For 15MeV, I_{4+} cross-section was calculated using equation 16, where the cross-section was independent of ERDA yields but depends on the thickness of the sample. Appendix D shows the tables for the measured and calculated values.

An experimental uncertainty of $\pm 8\%$ was estimated for ERDA yields. The relative uncertainty in the measured cross-section is $\pm 6\%$. In case where the Iodine energy beam is heavier than the target the scattering angle is not 40^{o}. So, the ratio of the scattered differential cross-section to the recoil differential cross-section was calculated with the same scattering angle of 40^{o} but only for targets heavier than iodine.

5.1.4 Foil thickness effect

Different yields value was tested with different composition sample with iodine energy beam ranging from 15MeV to 45MeV. The result for difference in the yield was minimal. Figure 17 shows the sample foil composition effect.

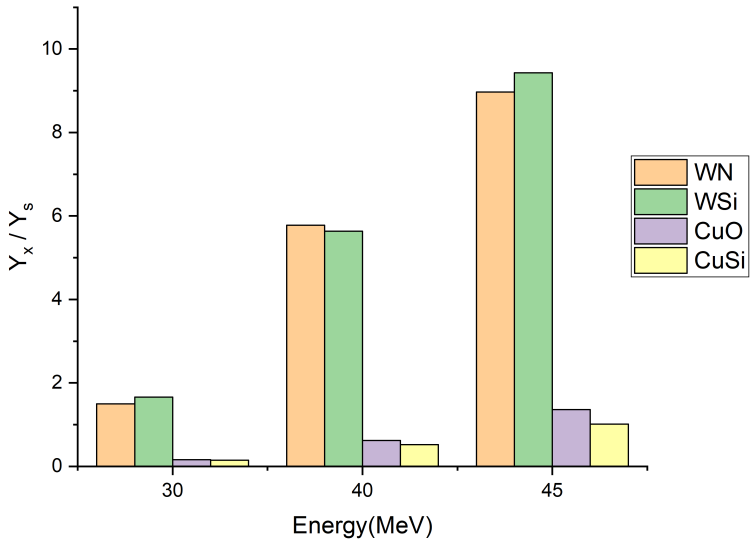

Figure 17: Ratio of yields for elements with different composition

5.2 Comparison between theory and experiment

The experimental results were compared with theoretical calculations of X-ray production cross-section calculated from ISICS11. Using DOSBox emulator, beam energy along with projectile and targets atoms were given to the ISICS11 software to get the theoretical X-ray production cross-section.

5.2.1 Recoil cross-section

Differential cross-section for recoils were calculated and used to calculate the x-ray production cross-section. In figures 18-21, the experimental data of production cross-section for Au, Cu, Nb, Ru, Ta, Ti, W and Zn in dependence of the bombarding energy in the range of 15-45MeV/u $^{126.9}$I beam are given.
In the comparison in figure 18, it was observed that the experimental data is not in full agreement with the theoretical predictions from PWBA and ECPSSR model. It was seen that for the elements Cu, Zn, Ru, Ti, Nb lighter than projectile beam, experimental x-ray cross-section were closed to ECPSSR-UA data where as for the heavier elements Ta, W and Au the experimental data lies in between but close to ECPSSR-UA data. This shows that some of the errors are not negligible in the measurement. The errors such as ion energy resolution, measurement spectral determination of the X-ray yield and beam current stability, number density of the thin film measurement, x-ray detector

efficiency, the reference data and so on. However, a pattern seems to be that for elements with higher Z than projectile the measured data are much closer to the ECPSSR prediction than elements with lower Z than the projectile. The significantly larger data for heavier elements than ECPSSR predictions was expected as ECPSSR overestimate the binding effect for heavier ions. (Fijał-Kirejczyk *et al.*, 2008)

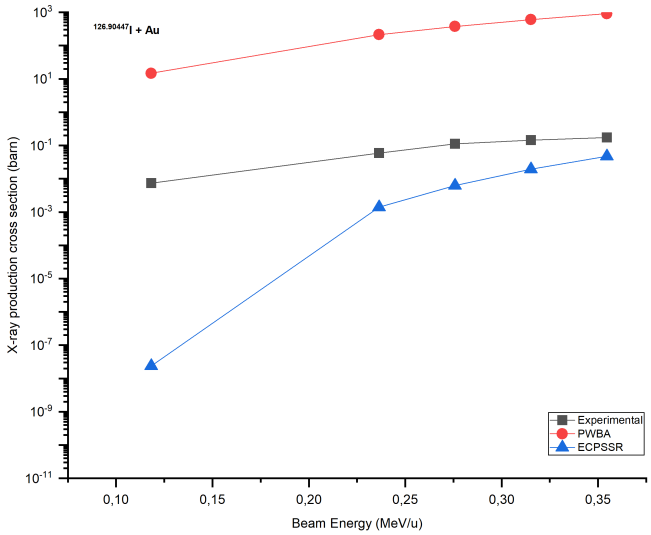

(a)

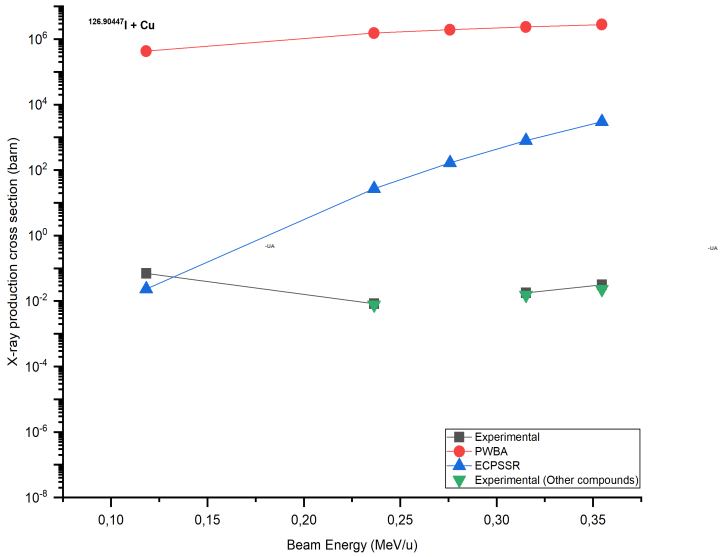

(b)

Figure 18: X-ray production cross-section with a) $^{196.97}$Au and b)$^{63.546}$Cu target elements in dependence of the bombardment energy

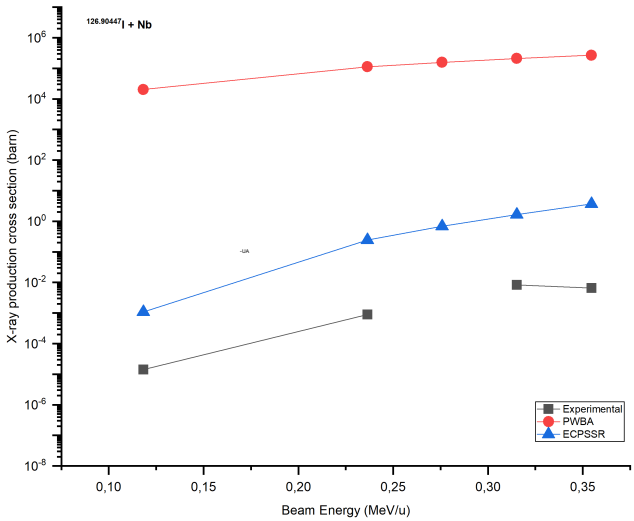

(a)

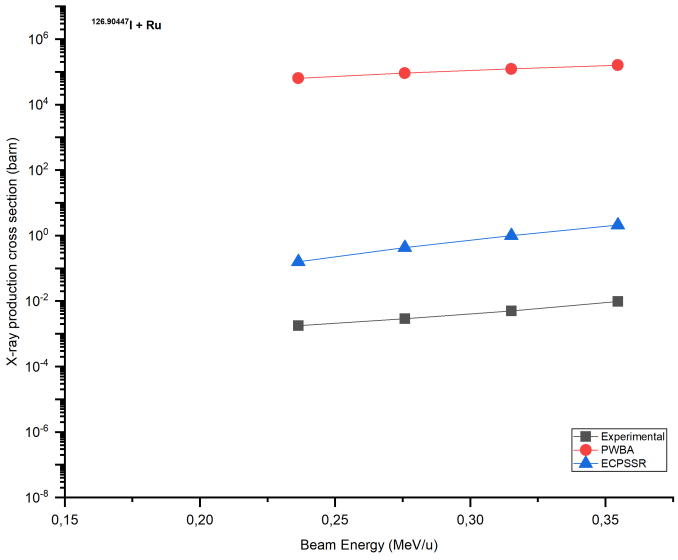

(b)

Figure 19: X-ray production cross-section with a) $^{92.906}$Nb and b) $^{101.07}$Ru target elements in dependence of the bombardment energy

From these figures we can speculate, three different processes in the projectile interaction with atoms having lower-Z (Ti, Cu, Zn), medium-Z (Nb, Ru) and higher-Z (Au, W, Ta) materials, respectively. The iodine ions fully interact with the electrons in all shells of the lower-Z materials and due to much energy remaining, is little deflected by the nucleus to pass by. In case of targets with higher-Z number, the ion partially

interacts with the electrons in some shells and lose most of its energy but being farther away from the nucleus gets mildly deflected. While for the materials with medium-Z, the ion fully interacts with the all electron shells to lose its most of energy at the most inner shell and is then strongly deflected due to a high closeness to the nucleus. Hence, in the case of medium-Z, simultaneous occurrence of high energy loss and strong deflection leads to strong perturbation to the target atom. Whereas, the ion deflection is weak or mild in case of higher-Z and lower-Z. Due to which the less energy is lost by the ion during the interaction with lower-Z and no interaction of ions occurs with the very inner electrons for the materials with higher-Z to cause lower perturbation. Therefore, for the cases of lower-Z and higher-Z cases, the simpler PWBA theory might be enough to describe the process, whereas for the medium-Z case, the ECPSSR could better describe the process.

However, in figures 18(b), 19(a), 19(b), 20(b), 21(b) targets elements with lower-Z than the projectiles have cross-section values reasonably lower than ECPSSR-UA theory whereas, in figures 18(a), 20(a), 21(a) the target elements with higher-Z than the projectile has cross-section values reasonably higher than ECPSSR-UA.

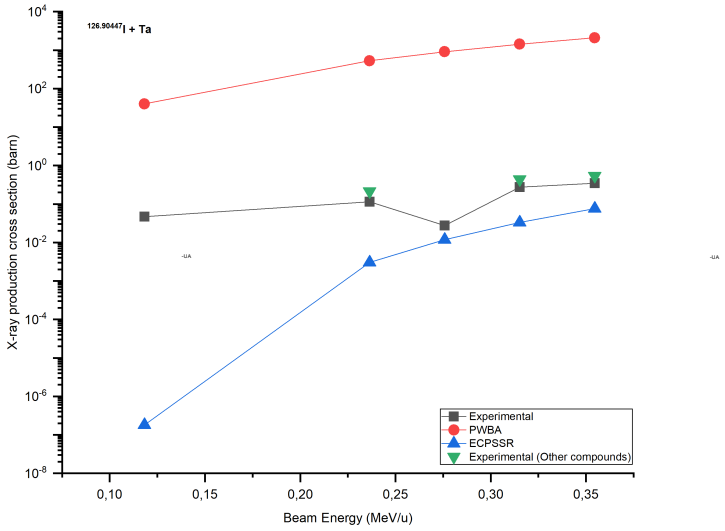

(a)

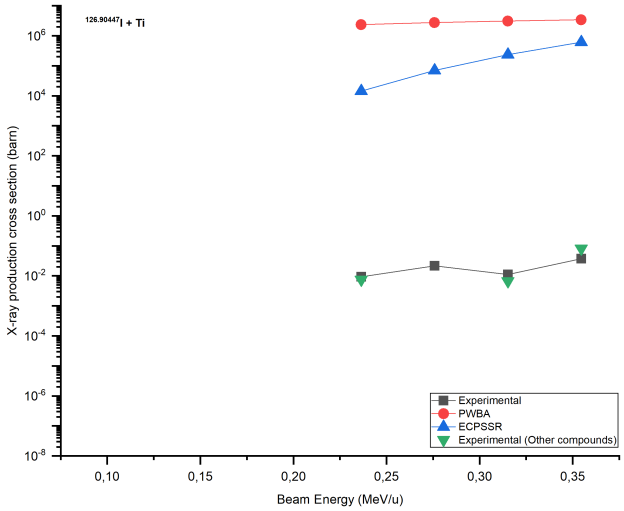

(b)

Figure 20: X-ray production cross-section with a) $^{180.95}$Ta and b)$^{47.867}$Ti target elements in dependence of the bombardment energy along with some compounds of target elements

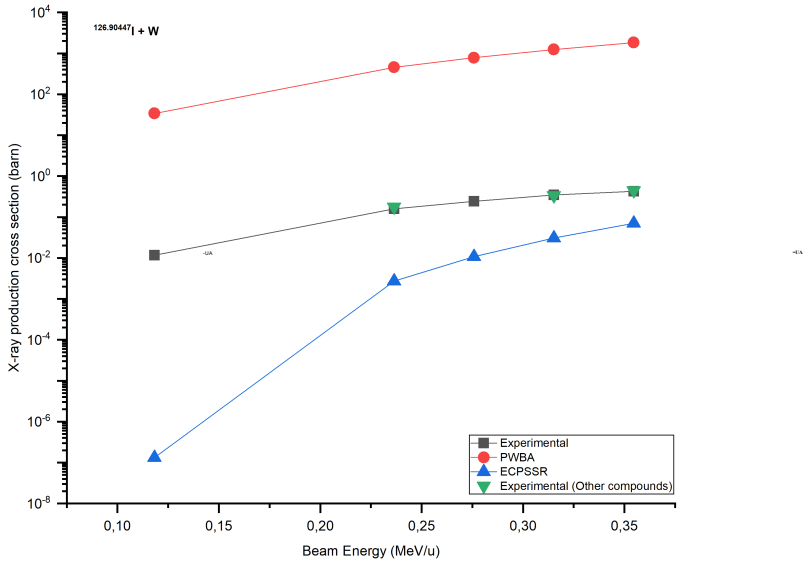

(a)

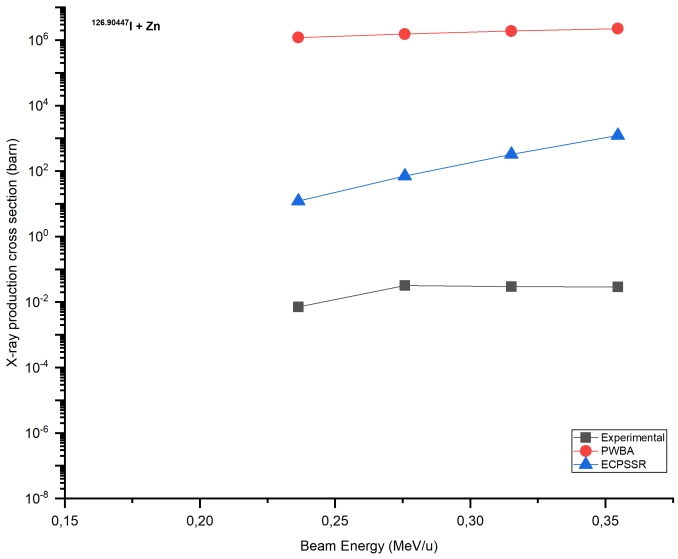

(b)

Figure 21: X-ray production cross-section with a) $^{183.84}W$ and b)$^{65.38}Zn$ target elements in dependence of the bombardment energy

For Ta, Au and W at higher energy even the basic ECPSSR theories give similar agreement with the experiment as by ECPSSR-UA as shown in figure 22(a)-22(b). The serious discrepancies were found particularly in the low energy range (15-30MeV) between the theoretical predictions and the existing data for the L-subshell ionization by heavier ions, which perturb the initial electronic state much stronger. The fact that the theoretical approaches neglect the coupling effects and treat the L-subshells independently, is the main reason for observed discrepancies between the theoretical predictions and the experimental data. The L-subshell ionization cross-section for heavy ions is substantially modified due to possible vacancy transfer between the subshell during collision (Fijał-Kirejczyk *et al.*, 2008).

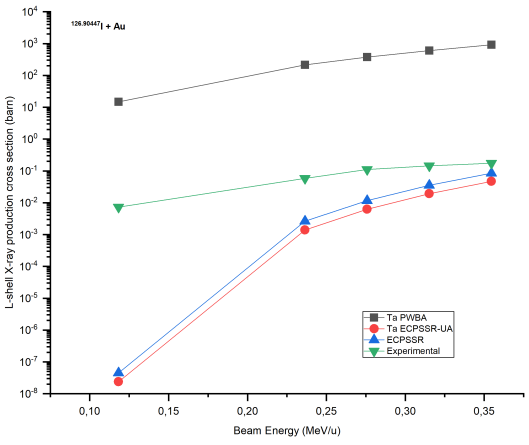

(a)

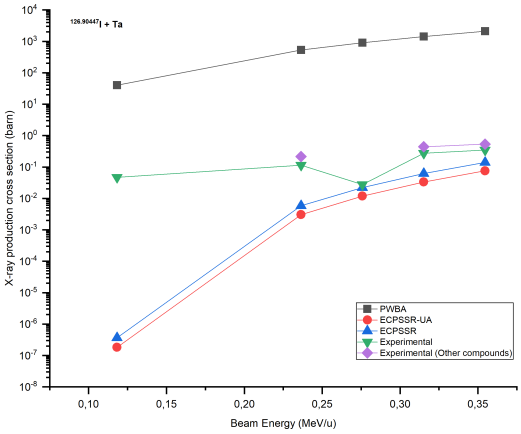

(b)

Figure 22: L-shell X-ray production cross-section with a) $^{196.97}$Au and b)$^{180.95}$Ta target elements in dependence of the bombardment energy with ECPSSR and ECPSSR-UA data

5.2.2 Comparison against reduced velocity parameters

The reduced velocity parameters for corresponding L_i subshell as adopted in ECPSSR approximation (Brandt and Lapicki, 1979a) is given by,

$$\xi_{L_i} = \frac{2v_1 n^2}{(\theta_{L_i} Z_{2L})} \tag{24}$$

where, v_1 is the projectile velocity, n is the principal quantum number of the L-shell electron (n = 2), $Z_{2L} = Z - 4.15$ is the effective nuclear charge of the target seen by the electron in the L-shell with Z being the target atomic number. $\theta_{L_i} = \frac{U_{L_i} n^2}{Z_{2L}^2 R_\infty}$ is the scaled binding energy, U_{L_i} and R_∞ are the observed binding energy for L_i subshell and Rydberg constant respectively. The "average" reduced L-shell velocity parameters is given by,

$$\xi_L = \frac{(\xi_{L_1} + \xi_{L_2} + 2\xi_{L_3})}{4} \tag{25}$$

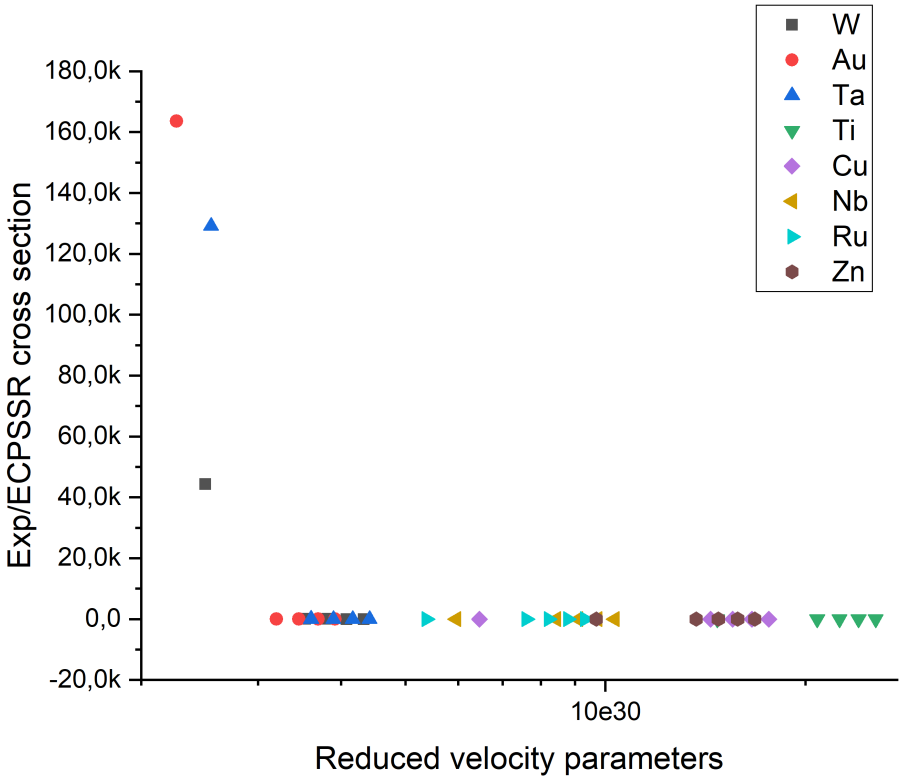

Figure 23: Average reduced velocity to ratio of experimental and ECPSSR cross-section production

Figure 23 shows the ratio between experimental and theoretical predictions for L, cross-section as a function of the logarithm of average reduced L-shell velocity parameter ξ_L. It can be seen that there is satisfactory agreement between the experimental Lα X-ray production to the predictions of ECPSSR.

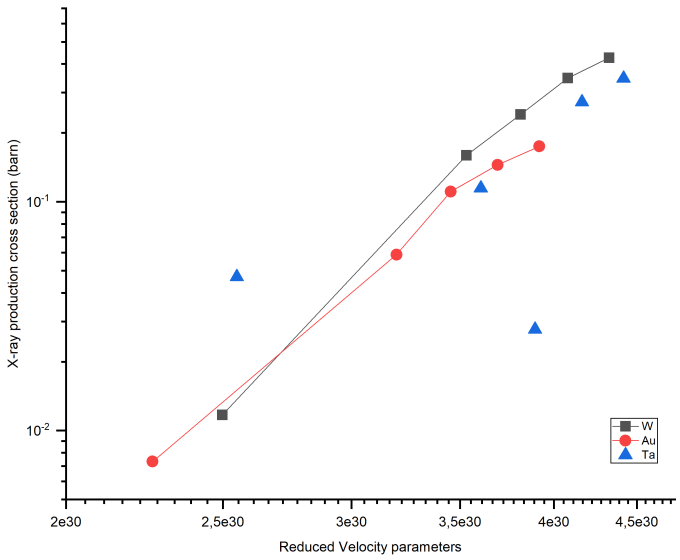

(a)

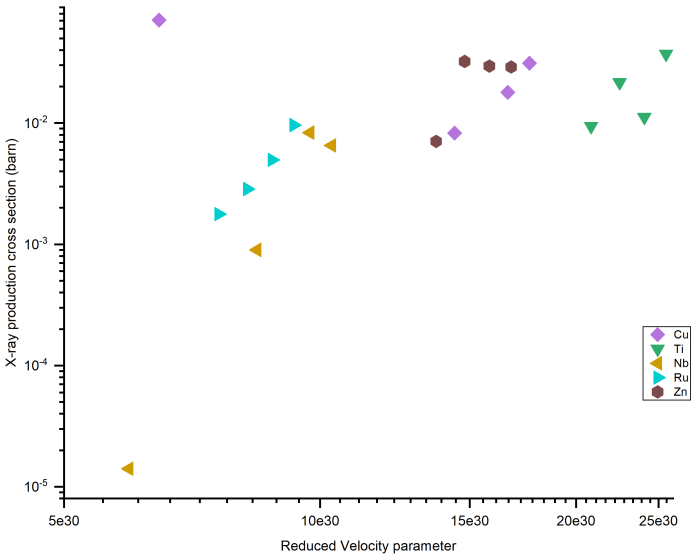

(b)

Figure 24: Average reduced velocity to experimental cross-section production (a) Heavier than projectiles (b) Lighter than projectiles

Figure 24, presents the logarithm of average velocity parameter to experimental x-ray production cross-section against the target elements heavier (a) than and lighter (b) than incident iodine ion respectively.

5.2.3 Scattered cross-section

Along with the differential cross-section for recoil elements, differential cross-section for scattered iodine was also calculated for heavy target elements. Figure 22 shows the comparison of the experimental data and theoretical calculations of x-ray production cross-section for scattered iodine due to W, Au and Ta.

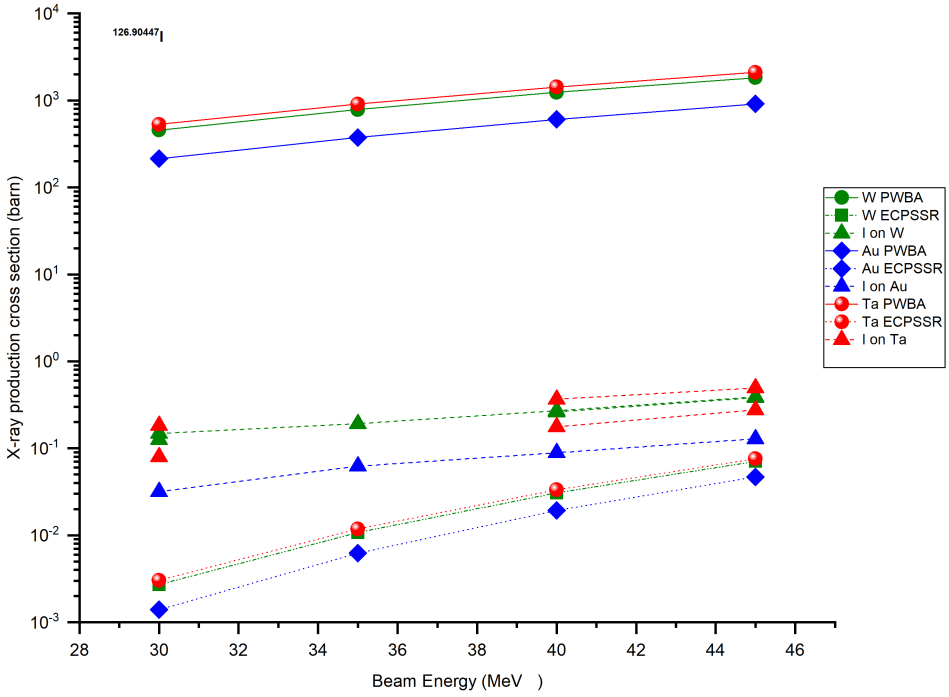

Figure 25: X-ray production cross-section for scattered iodine

6 Conclusion and outlook

Backscattered ions technique though is the origin of ion backscattering spectrometry and analytical technique like Particle induced X-ray Emission (PIXE) which is based on characteristics X-rays emission, moreover when high energy heavy ions are used as projectiles, various results were observed. The modern accelerator used made it feasible for the production of these high energy iodine ions. As the mass of the projectile was bigger, larger value of the ionization cross-section was obtained. As Iodine ions can penetrate more deeply in the target more precise and detail measurement of the sample were made.

ERDA data were also collected along with the X-ray data, which were further used to calculate the thickness of the target material in the sample used. Thus, obtained thickness were used to calculate the X-ray production cross-section for 15MeV iodine beam energy. Besides, thickness recoil and scattering yields were measured using POTKU software. In addition to the X-ray production cross-section, differential recoil cross-section and differential scattering cross-section were also calculated.

Thus, obtained X-ray production cross-sections were compared with the data obtained from PWBA, ECPSSR and ECPSSR-UA using the ISICS11 software. The experimental data showed significant discrepancies with the theoretical data. However, in making the comparisons, the fact that semi-empirical values for fluorescence and

Coster-Kronig yields of Krause (Krause, 1979), have reported uncertainties of 5 to 20% adopted in the conversion from the theoretical ECPSSR ionization cross-section to the X-ray production cross-section.
Furthermore, as a final test of goodness of the theories a comparison of the reduced velocity against the ratio of the experimental to theoretical x-ray production cross-section was computed.
Hence, extensive theoretical studies in the direction to include intra-shell coupling and effect of electron capture by the incoming ions should also be considered.

ACKNOWLEDGEMENTS

I wish to thank my supervisor Kenichiro Mizohata, Professor Jyrki Räisänen for their professional guidance and all the help I received over the years. Without their support during this long time this thesis would not have been completed.

I would like to thank Head of Academic Affairs at University of Helsinki, Anne Palo-Kauppi and Tiina Hasari for their help.

I want to thank my Mum, Dad, brother, mama Rajendra and baba for everything. I also thank my friend and all other people for their encouragement, they know who they are. Finally, I would like to thank Narmin for her loving presence, patience and continuous support during this work.

REFERENCES

(University of Helsinki), K. M. T. N. and J. R. (2017) 'Heavy ion induced X-ray production cross sections'.

Accelerator Laboratory | Faculty of Science | University of Helsinki (no date). Available at: https://www.helsinki.fi/en/faculty-of-science/faculty/physics/research/materials-physics/accelerator-laboratory (Accessed: 13 January 2019).

Birks, L. S. *et al.* (1964) 'Excitation of Characteristic X Rays by Protons, Electrons, and Primary X Rays', *Journal of Applied Physics*, 35(9), pp. 2578–2581. doi: 10.1063/1.1713803.

Brandt, W. and Lapicki, G. (1979a) 'L-shell Coulomb ionization by heavy charged particles', *Physical Review A*, 20(2), pp. 465–480. doi: 10.1103/PhysRevA.20.465.

Brandt, W. and Lapicki, G. (1979b) 'L -shell Coulomb ionization by heavy charged particles', *Physical Review A*. American Physical Society, 20(2), pp. 465–480. doi: 10.1103/PhysRevA.20.465.

Brandt, W. and Lapicki, G. (1981) 'Energy-loss effect in inner-shell Coulomb ionization by heavy charged particles', *Physical Review A*. American Physical Society, 23(4), pp. 1717–1729. doi: 10.1103/PhysRevA.23.1717.

Chadwick, J. (1912) 'LIV. The γ rays excited by the β rays of radium', *Philosophical Magazine*. Taylor & Francis, 24(142), pp. 594–600. doi: 10.1080/14786441008637362.

Cipolla, S. J. (2007) 'An improved version of ISICS: a program for calculating K-, L- and M-shell cross sections from PWBA and ECPSSR theory using a personal computer', *Computer Physics Communications*, 176(2), pp. 157–159. doi: 10.1016/j.cpc.2006.08.004.

Fijał-Kirejczyk, I. *et al.* (2008) 'Coupling and binding-saturation effects in L -subshell ionization of heavy atoms by 0.3-1.3-MeV/amu Si ions', *Physical Review A - Atomic, Molecular, and Optical Physics*, 77(3), pp. 1–15. doi: 10.1103/PhysRevA.77.032706.

Gove, H. E. (1969) 'Particle Acceleration. J. Rosenblatt. Methuen, London, 1968 (U. S. distributor, Barnes and Noble, New York). viii + 183 pp., illus. $5.50. Methuen's Monographs on Physical Subjects', *Science*. American Association for the Advancement of Science, 164(3881), pp. 818–819. doi: 10.1126/science.164.3881.818-a.

Hansteen, J. M. *et al.* (2017) 'Experimental measurements of X-ray production cross-sections by protons of energies between 1 and 2.3 MeV and comparison with theoretical predictions of PWBA and ECPSSR models', *Nuclear Instruments and Methods in Physics Research, Section B: Beam Interactions with Materials and Atoms*. Elsevier B.V., 161(4), pp. 141–144. doi: 10.1016/S0168-583X(99)00916-7.

Ion Beam Sources Archives - National Electrostatics Corp. (no date). Available at:

http://www.pelletron.com/product-category/ion-beam-sources/ (Accessed: 13 January 2019).
Ishii, K. (1995) 'High energy limit of atomic bremsstrahlung', *Nuclear Instruments and Methods in Physics Research Section B: Beam Interactions with Materials and Atoms*. North-Holland, 99(1–4), pp. 163–165. doi: 10.1016/0168-583X(94)00571-0.

Ishii, K. *et al.* (2005) 'Contribution of atomic bremsstrahlung in PIXE spectra and screening effect in atomic bremsstrahlung', *X-Ray Spectrometry*. John Wiley & Sons, Ltd, 34(4), pp. 363–365. doi: 10.1002/xrs.838.

Ishii, K. and Morita, S. (1984) 'Continuum x rays produced by light-ion—atom collisions', *Physical Review A*. American Physical Society, 30(5), pp. 2278–2286. doi: 10.1103/PhysRevA.30.2278.

Johansson, S. A. E. (1989) 'PIXE: a novel technique for elemental analysis', *Endeavour*, 13(2), pp. 48–53. doi: 10.1016/0160-9327(89)90002-1.

Krause, M. O. (1979) 'Atomic radiative and radiationless yields for *K* and *L* shells', *Journal of Physical and Chemical Reference Data*. American Institute of Physics for the National Institute of Standards and Technology, 8(2), pp. 307–327. doi: 10.1063/1.555594.

Lapicki, G. (2005) 'The status of theoretical K-shell ionization cross sections by protons', *X-Ray Spectrometry*. John Wiley & Sons, Ltd., 34(4), pp. 269–278. doi: 10.1002/xrs.837.

Lapicki, G. G. *et al.* (1981) 'Energy-loss effect in inner-shell Coulomb ionization by heavy charged particles', *Physical Review A*. Elsevier Ltd, 22(4), pp. 722–724. doi: 10.1088/0031-8949/76/6/021.

Lapicki, G., Laubert, R. and Brandt, W. (1980) 'Coulomb-deflection effect in inner-shell ionization by heavy charged particles', *Physical Review A*. American Physical Society, 22(5), pp. 1889–1895. doi: 10.1103/PhysRevA.22.1889.

Lapicki, G. and Losonsky, W. (1979) 'Coulomb deflection in ion-atom collisions', 20(2).
Manpuneet Kaur, Harsh Mohan, Arvind K. Jain, Parjit S. Singh, and S. S. (2017) 'Influence of Multiple Ionization on L X-ray intensity ratio induced by proton', *International Journal of Pure and Applied Physics*, 13(1), pp. 77–74.

Mizohata, K. (2012) *Progress in Elastic Recoil Detection Analysis*. Available at: https://helda.helsinki.fi/handle/10138/37680.

Mokuno, Y. *et al.* (1998) 'High energy resolution PIXE analysis using focused MeV heavy ion beams', *Nuclear Instruments and Methods in Physics Research Section B: Beam Interactions with Materials and Atoms*, 136–138(97), pp. 368–372. doi: 10.1016/S0168-583X(97)00708-8.

Mukoyama, T. and Sarkadi, L. (1981) 'L-shell ionization by low-energy protons and alpha particles', *Nuclear Instruments and Methods in Physics Research*. North-Holland, 190(3), pp. 619–626. doi: 10.1016/0029-554X(81)90963-0.

Murozono, K. *et al.* (1999) 'PIXE spectrum analysis taking into account bremsstrahlung spectra', *Nuclear Instruments and Methods in Physics Research Section B: Beam Interactions with Materials and Atoms*. North-Holland, 150(1–4), pp. 76–82. doi: 10.1016/S0168-583X(98)00918-5.

Nejedly, Z., Campbell, J. L. and Gama, S. (2004) 'An Excel utility for the rapid characterization of "funny filters" in PIXE analysis', *Nuclear Instruments and Methods in Physics Research Section B: Beam Interactions with Materials and Atoms*, 219–220, pp. 136–139. doi: 10.1016/j.nimb.2004.01.041.

Romo-Kröger, C. M. (2010) 'How the sensitivity in PIXE elemental analysis is affected by the type of particle, cross-sections, background radiation and other factors?', *Vacuum*, 84(10), pp. 1250–1253. doi: 10.1016/j.vacuum.2009.10.035.

Roumié, M. *et al.* (2005) 'Application of PIXE using Al funny filter for cluster analysis of Byzantine amphorae from Beirut', *Nuclear Instruments and Methods in Physics Research, Section B: Beam Interactions with Materials and Atoms*, 227(4), pp. 584–590. doi: 10.1016/j.nimb.2004.09.017.

T.B. Johansson, R. Akselsson, S. A. E. J. (1970) 'X-ray analysis: Elemental trace analysis at the 10−12 g level', *Nuclear Instruments and Methods*. North-Holland, 84(1), pp. 141–143. doi: 10.1016/0029-554X(70)90751-2.

Ultra-LEGe Detector Features (no date). Available at: http://www.canberra.com (Accessed: 5 August 2019).

Watson, V. H. and R. L. (no date) 'https://cyclotron.tamu.edu/progress-reports/1999-2000/sec4/4s.pdf'.

Yamadera, A. *et al.* (1981) 'Quasifree-electron bremsstrahlung induced by the projectile field', *Physical Review A*. American Physical Society, 23(1), pp. 24–33. doi: 10.1103/PhysRevA.23.24.

APPENDICES

Appendix A: ISICS11

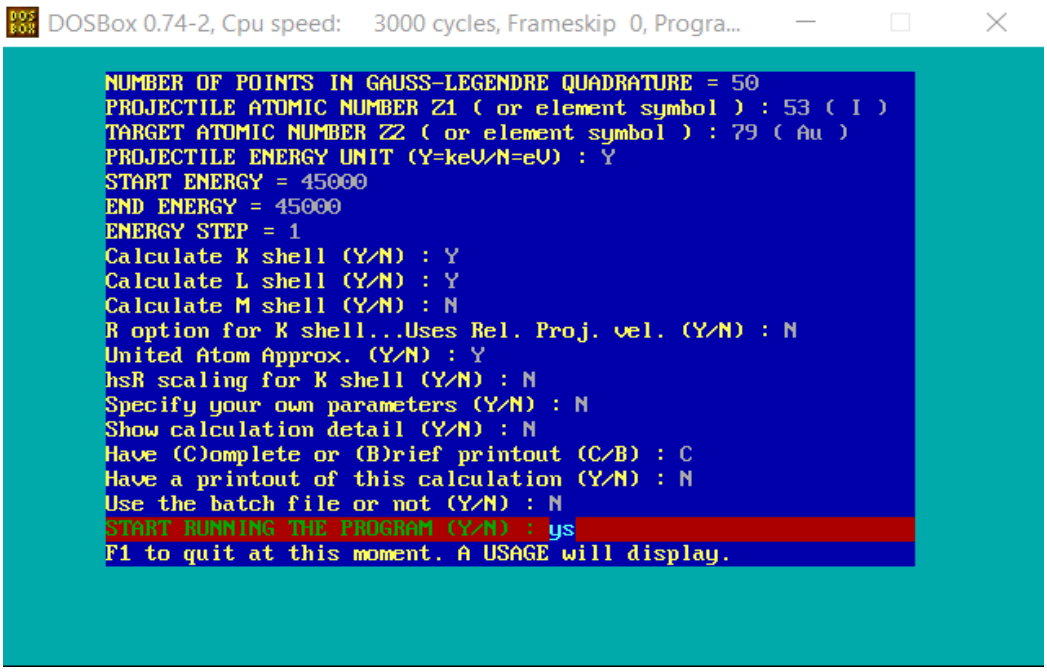

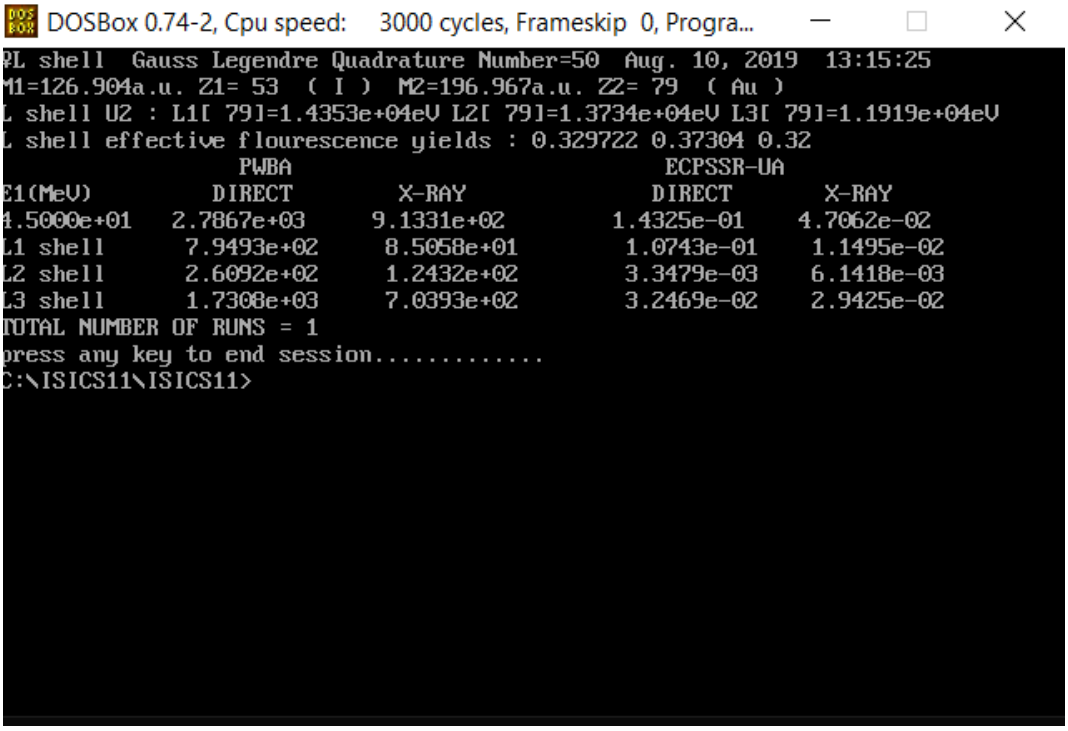

Appendix B: R and Origin Pro, Python code snippets

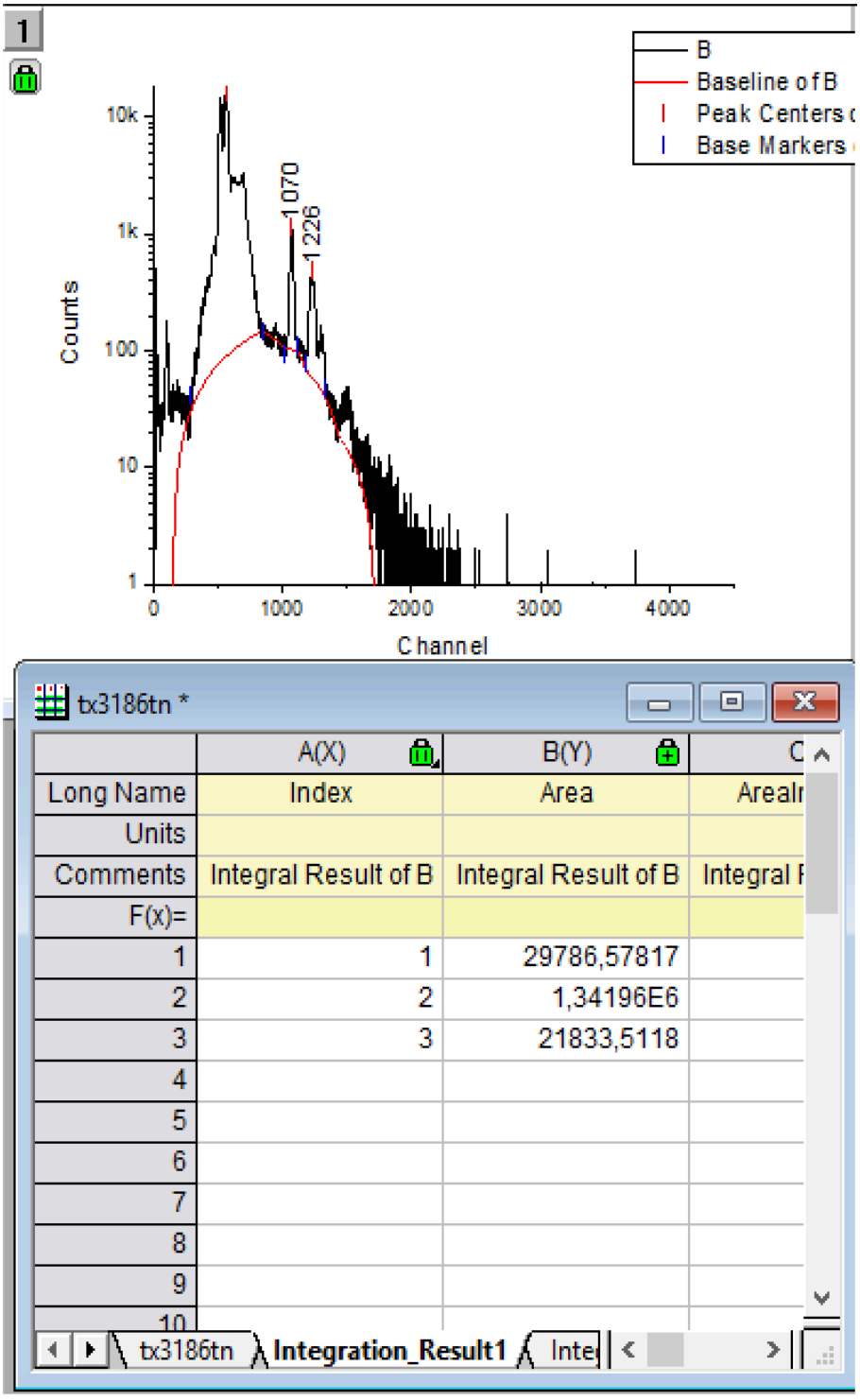

tx3186tn *

	A(X)	B(Y)	C
Long Name	Index	Area	Areal
Units			
Comments	Integral Result of B	Integral Result of B	Integral F
F(x)=			
1	1	29786,57817	
2	2	1,34196E6	
3	3	21833,5118	
4			
5			
6			
7			
8			
9			
10			

tx3186tn | Integration_Result1 | Inte

```
library(ggplot2)
p11<-ggplot(data=tx3183tn, aes(x=tx3183tn$X0 ,
y=tx3183tn$X0.1))+scale_y_log10()+geom_line(size=0.1)+ xlab("Energy [keV]") +
ylab("Counts")+ scale_x_continuous(limits = c(0, NA), expand = c(0,0))
p11
Xlabel<-tx3183tn$X0
Elabel<-(7.59/10^3) * Xlabel + 9.24/10^3
p11<-ggplot(data=tx3183tn, aes(x=Elabel ,
y=tx3183tn$X0.1))+scale_y_log10()+geom_line(size=0.1)+ xlab("Energy [keV]") +
ylab("Counts")+ scale_x_continuous(limits = c(0, NA), expand = c(0,0))
p11
tx3183tn$Xlabel<-Elabel
View(tx3183tn)
p11 + theme_light()
legends_coord<-locator(1)
plot(p11)
identify(tx3183tn$X0, tx3183tn$X0.1)
plot(tx3183tn$X0, log10(tx3183tn$X0.1), type = "l")


while True:
    num1 = float(input("Give Z: "))
    num2 = float(input("Give E: "))

    print("Differential cross-section is: ", 265.2872243 * (num1/num2) * (num1/num2))
    continue
```

Appendix C: Measured X-ray production cross-section production and thickness from ERDA

40MeV, I 7+							
Specimen	YxKa(la)	YxKb	Yx(kb + kg)(lb)	Yx(l) background	Ys(recoils)	dσs/dΩ(barn/str)(recoils)	Ys(scattering)(l)
tx3182, AlO						2802.096309	
tx3183, WN	18241,81168000		13806,6032800		5546	315,8485759	21134
tx3184, CuO	5007,44472		0		8099	152,4981073	2036
tx3185, Cu on Si	7679,90009		0		14692	152,4981073	13906
tx3186, Ta2O5	28847,59197		20825,06747	1972,29054	10765	311,3924258	47328
tx3187, TiO2	2341,157751	*****	0		5173	130,2545758	816
tx3188, W on Si	8237,92492		5670,7363		2468	315,8485759	8863
tx3189, Au on Si	12448,18123		8652,28708	1338,39216	9421	340,6407802	46587
tx3190, NbC(IAEA)	662,4380631		0		2862	189,9592555	4559
tx3191, RuO2(IAEA	289,74675		0		2209	198,8462493	3644
tx3192,Ta2O3	16628,57781		10782,54086	978,83389	3694	311,3924258	12533
tx3193, TiN	684,6432553	*****	0		2523	130,2545758	956
tx3194,ZnO	2449,68946		0		2478	157,152787	921
tx3195, TiO2	1310,315873	*****	0		3708	130,2545758	837
35MeV, I 6+							
tx3305, AlO							
tx3306, W on Si	10160,32458		7802,505	1391,47408	5856	412,5369155	21075
tx3307, Au on Si	7538,08726		4450,13501	475,18446	9137	444,9185701	49442
tx3308, NbO					6260		9472
tx3309, RuO2(IAEA	424,7834		0			259,7175501	
tx3310, Ta2O5(IAE	13437,58985		10160,01899	1126,37931		406,7166378	
tx3311, TiN(IAEA)	2517,713904	****	0		3754	170,1284256	1180
tx3312, ZnO(IAEA)	2032,88152		0			205,260783	
30MeV, I 5+							
tx3226, WN	12453,18779		9308,98314	1042,73599	14537	561,5085794	52839
tx3227, CuO	2431,8161		0		15189	271,1077462	4421
tx3228, Ta2O5	17660,00311		12147,04388	1226,48741	27310	553,5865347	111511
tx3229, TiO2	2404,193023	****	0		11267	231,5636903	3100
tx3230,Cu Si	5315,33068		0		35621	271,1077462	45637
tx3231,W Si	8903,28587		6902,84501	956,27836	9509	561,5085794	32684
tx3232, Au on Si	8669,87122		4540,83181	701,19261	25868	605,5836092	145237
tx3233, NbO(IAEA)	117,42749		0		8378	337,705343	12714
tx3234,RuO2(IAEA	127,72747		0		4840	353,5044432	7918
tx3235, Ta2O5(IAE	5422,33251		4380,59356	375,73934	4822	553,5865347	16017
tx3236, TiN(IAEA)	1025,892857		0		5942	231,5636903	2843
tx3237, Zn	1794,34878		0		13494	279,3827325	5180
tx3238, Al							
45MeV, I 8+							
tx3240, WN	21708,86691		13930,1729	1930,5247	3973	249,5593686	12715
tx3241, CuO	4805,31081		0		3530	120,4923316	971
tx3242, Ta2O5	37570,43784		22665,78029	2422,65319	8139	246,038486	28903
tx3243, TiO2	4888,665846	****	0		2577	102,9171957	488
tx3244, Cu on Si	13986,71834		0		13851	120,4923316	12391
tx3245, W on Si	13599,65889		9007,97226	1278,48089	2397	249,5593686	7903
tx3246, Au on Si	13261,59236		8248,20776	1716,84533	6296	269,1482708	25921
tx3247, NbO(IAEA)	1439,78795		0		6296	150,0912636	9740
tx3248, RuO2(IAEA	1678,33856		0		5209	157,1130859	8524
tx3249, Ta2O(IAEA	25639,46128		15396,71238	1329,64687	3573	246,038486	11036
tx3250, TiN	5856,646633		0		1404	102,9171957	432
tx3251, ZnO	3870,36567		0		3147	124,1701033	972
15Mev, I 4+							
tx3313, W on Si	3023,47944		2175,7952				
tx3314, Au on Si	2770,21627		1191,62071				
tx3315, NbO(IAEA)	8,52765						
tx3316, Cu on Si	5287,06563						
tx3317, Ta2O5	4509,93095		2192,81704	220,37982			
tx3242, Ta2O5(sma	1756,26873						

dσs/dΩ(barn/str) scatterir	Ωerd/Ωxray	$\sigma = \frac{Y_s}{\epsilon} \frac{\Omega}{Y_s} \frac{\partial \sigma_s(E,\theta)}{\partial \Omega}$	YX= YxKa+Yx(kb+kg)	YX/Ys	ratio(Isca/Erec)	Cross-section for Iodine scattered from heavy elements
	0,021590909					
907,9455251		0,34678413	32048,41496000	5,778653978	2,874622824	0,2616003
		0,017914423	5007,44472000	0,618279383	0	0
		0,015145817	7679,90009000	0,52272666	0	0
883,5722614		0,273001494	49672,65944000	4,614273984	2,837487968	0,17619555
		0,011200432	2341,15775125	0,45257254	0	0
907,9455251		0,338199295	13908,66122000	5,63560017	2,874622824	0,27071852
1034,785979		0,144959049	21100,46831000	2,239727026	3,037763061	0,0890495
		0,008353908	662,43806306	0,23145984	0	0
		0,004955573	289,74675000	0,131166478	0	0
883,5722614		0,439027287	27411,11867000	7,420443603	2,837487968	0,36717017
		0,006715737	684,64325530	0,271360783	0	0
		0,029517897	2449,68946000	0,988575246	0	0
		0,008745464	1310,31587302	0,35337537	0	0
1185,888033		0,240430799	17962,82958000	3,067423084	2,874622824	0,19204564
1351,557197		0,110913726	11988,22227000	1,312052344	3,037763061	0,0622654
		0	0,00000000	0		0
		2,86E-03	424,78340000		0	
1154,053566		2,77E-02	23597,60884000		2,837487968	
	2,39E-02	0,021679167	2517,71390374	0,670674988	0	0
		3,22E-02	2032,88152000		0	
1614,125378		0,159711954	21762,17093000	1,497019394	2,874622824	0,12631022
		0,008247021	2431,81610000	0,160103766	0	0
1570,795131		0,114798542	29807,04699000	1,091433431	2,837487968	0,07977639
		0,00938826	2404,19302266	0,2133836	0	0
		0,007686342	5315,33068000	0,149219019	0	0
1614,125378		0,177337558	15806,13088000	1,662228508	2,874622824	0,14831369
1839,619519		0,058761218	13210,70303000	0,510696731	3,037763062	0,03179291
		0,000899334	117,42749000	0,014016172	0	0
		0,001772505	127,72747000	0,026389973	0	0
1570,795131		0,21382951	9802,92607000	2,032958538	2,837487968	0,18266179
		0,007596148	1025,89285714	0,172651104	0	0
		0,007058612	1794,34878000	0,132973824	0	0
717,3890569		0,425338709	35639,03981000	8,970309542	2,874622824	0,38204804
		0,031164473	4805,31081000	1,36127785	0	0
698,1311695		0,345973867	60236,21813000	7,400936003	2,837487667	0,27644288
		0,03709518	4888,66584623	1,897037581	0	0
		0,023117864	13986,71834000	1,009798451	0	0
717,3890569		0,447213087	22607,63115000	9,431635857	2,874622824	0,38991633
817,608675		0,174709633	21509,80012000	3,416423145	3,037763061	0,12890914
		0,00652143	1439,78795000	0,228682965	0	0
		0,009618142	1678,33856000	0,322199762	0	0
698,1311695		0,536896397	41036,17366000	11,48507519	2,837487667	0,49322581
		0,081568685	5856,64663300	4,171400736	0	0
		0,029015222	3870,36567000	1,229858808	0	0
		1,17E-02	5199,27464000			
		7,32E-03	3961,83698000			
		1,41E-05	8,52765000			
		7,05E-02	5287,06563000			
		4,70E-02	6702,74799000			

		Energy(MeV)	WN	W on SI	CuO	Cu on Si			
		15							
		30	1,497019394	1,66222851	0,16010377	0,149219019			
		40	5,778653978	5,63560017	0,61827938	0,52272666			
		45	8,970309542	9,43163586	1,36127785	1,009798451			
		Mass of iodine(I	2,11E-25			**Rydberg Constant (**	1,10E+07		eV
E(MeV)	E(J)	**σ(barn) W**	Z=74	**L**	ECPSSR	**σ(barn) W/ECPSSR**	**Velocity(v)**	**Z-4,15**	U1*1,6022E-19
15	2,4033E-12	0,011717004					4772849,755	69,85	1,21E+04
30	4,8066E-12	0,159711954	0,177337558				6749828,855	69,85	
35	5,6077E-12	0,240430799					7290648,428	69,85	
40	6,4088E-12	0,34678413	0,338199295				7794031,013	69,85	
45	7,2099E-12	0,425338709	0,447213087				8266818,273	69,85	
	0						0		
	0	**σ(barn) Au**	Z= 79				0		
15	2,4033E-12	7,32E-03					4772849,755	74,85	1,44E+04
30	4,8066E-12	0,058761218					6749828,855	74,85	
35	5,6077E-12	0,110913726					7290648,428	74,85	
40	6,4088E-12	0,144959049					7794031,013	74,85	
45	7,2099E-12	0,174709633					8266818,273	74,85	
	0						0		
	0	**σ(barn) Ta**	Z= 73				0		
15	2,4033E-12	4,70E-02					4772849,755	68,85	1,17E+04
30	4,8066E-12	0,114798542	0,21382951				6749828,855	68,85	
35	5,6077E-12	2,77E-02					7290648,428	68,85	
40	6,4088E-12	0,273001494	0,439027287				7794031,013	68,85	
45	7,2099E-12	0,345973867	0,536896397				8266818,273	68,85	
	0						0		
	0	**σ(barn) Ti**	Z= 22				0		
15	2,4033E-12						4772849,755	17,85	5,64E+02
30	4,8066E-12	0,00938826	0,007596148				6749828,855	17,85	
35	5,6077E-12	0,021679167					7290648,428	17,85	
40	6,4088E-12	0,011200432	0,006715737	0,00874546			7794031,013	17,85	
45	7,2099E-12	0,03709518	0,081568685				8266818,273	17,85	
	0						0		
	0	**σ(barn) Cu**	Z= 29				0		
15	2,4033E-12	7,05E-02					4772849,755	24,85	1,10E+03
30	4,8066E-12	0,008247021	0,007686342				6749828,855	24,85	
35	5,6077E-12						7290648,428	24,85	
40	6,4088E-12	0,017914423	0,015145817				7794031,013	24,85	
45	7,2099E-12	0,031164473	0,023117864				8266818,273	24,85	
	0						0		
	0	**σ(barn) Nb**	Z= 41				0		
15	2,4033E-12	1,41E-05					4772849,755	36,85	2,70E+03
30	4,8066E-12	0,000899334					6749828,855	36,85	
35	5,6077E-12						7290648,428	36,85	
40	6,4088E-12	0,008353908					7794031,013	36,85	
45	7,2099E-12	0,00652143					8266818,273	36,85	
	0						0		
	0	**σ(barn) Ru**	Z= 44				0		
15	2,4033E-12						4772849,755	39,85	3,22E+03
30	4,8066E-12	0,001772505					6749828,855	39,85	
35	5,6077E-12	2,86E-03					7290648,428	39,85	
40	6,4088E-12	0,004955573					7794031,013	39,85	
45	7,2099E-12	0,009618142					8266818,273	39,85	
	0						0		
	0	**σ(barn) Zn**	Z=30				0		
15	2,4033E-12						4772849,755	25,85	1,19E+03
30	4,8066E-12	0,007058612					6749828,855	25,85	
35	5,6077E-12	3,22E-02					7290648,428	25,85	
40	6,4088E-12	0,029517897					7794031,013	25,85	
45	7,2099E-12	0,029015222					8266818,273	25,85	

	L1				L2				L3	
U1	ξ1		U1*1,6022E-19	U2	ξ2		U1*1,6022E-19	U3	2ξ	ξ=0.25(ξ1 + ξ2 + ξ3)
1,94E-15	3,78E+30		1,15E+04	1,85E-15	3,97E+30		1,02E+04	1,64E-15	2,24E+30	2,50E+30
1,94E-15	5,35E+30			1,85E-15	5,61E+30			1,64E-15	3,17E+30	3,53E+30
1,94E-15	5,78E+30			1,85E-15	6,06E+30			1,64E-15	3,43E+30	3,82E+30
1,94E-15	6,18E+30			1,85E-15	6,48E+30			1,64E-15	3,66E+30	4,08E+30
1,94E-15	6,55E+30			1,85E-15	6,87E+30			1,64E-15	3,88E+30	4,33E+30
2,30E-15	3,42E+30		1,37E+04	2,20E-15	3,57E+30		1,19E+04	1,91E-15	2,06E+30	2,26E+30
2,30E-15	4,83E+30			2,20E-15	5,05E+30			1,91E-15	2,91E+30	3,20E+30
2,30E-15	5,22E+30			2,20E-15	5,46E+30			1,91E-15	3,14E+30	3,45E+30
2,30E-15	5,58E+30			2,20E-15	5,83E+30			1,91E-15	3,36E+30	3,69E+30
2,30E-15	5,92E+30			2,20E-15	6,19E+30			1,91E-15	3,56E+30	3,92E+30
1,87E-15	3,86E+30		1,11E+04	1,78E-15	4,05E+30		9,88E+03	1,58E-15	2,28E+30	2,55E+30
1,87E-15	5,46E+30			1,78E-15	5,73E+30			1,58E-15	3,23E+30	3,61E+30
1,87E-15	5,90E+30			1,78E-15	6,19E+30			1,58E-15	3,49E+30	3,89E+30
1,87E-15	6,31E+30			1,78E-15	6,62E+30			1,58E-15	3,73E+30	4,16E+30
1,87E-15	6,69E+30			1,78E-15	7,02E+30			1,58E-15	3,95E+30	4,42E+30
9,03E-17	2,08E+31		4,62E+02	7,39E-17	2,53E+31		4,56E+02	7,30E-17	1,28E+31	1,47E+31
9,03E-17	2,93E+31			7,39E-17	3,58E+31			7,30E-17	1,82E+31	2,08E+31
9,03E-17	3,17E+31			7,39E-17	3,87E+31			7,30E-17	1,96E+31	2,25E+31
9,03E-17	3,39E+31			7,39E-17	4,14E+31			7,30E-17	2,10E+31	2,41E+31
9,03E-17	3,59E+31			7,39E-17	4,39E+31			7,30E-17	2,22E+31	2,55E+31
1,76E-16			9,51E+02	1,52E-16	1,71E+31		9,31E+02	1,49E-16	8,75E+30	6,47E+30
1,76E-16	2,10E+31			1,52E-16	2,42E+31			1,49E-16	1,24E+31	1,44E+31
1,76E-16	2,27E+31			1,52E-16	2,62E+31			1,49E-16	1,34E+31	1,56E+31
1,76E-16	2,43E+31			1,52E-16	2,80E+31			1,49E-16	1,43E+31	1,66E+31
1,76E-16	2,57E+31			1,52E-16	2,97E+31			1,49E-16	1,51E+31	1,76E+31
4,32E-16	8,95E+30		2,46E+03	3,95E-16	9,80E+30		2,37E+03	3,80E-16	5,09E+30	5,96E+30
4,32E-16	1,27E+31			3,95E-16	1,39E+31			3,80E-16	7,20E+30	8,43E+30
4,32E-16	1,37E+31			3,95E-16	1,50E+31			3,80E-16	7,78E+30	9,11E+30
4,32E-16	1,46E+31			3,95E-16	1,60E+31			3,80E-16	8,32E+30	9,73E+30
4,32E-16	1,55E+31			3,95E-16	1,70E+31			3,80E-16	8,82E+30	1,03E+31
5,17E-16	8,10E+30		2,97E+03	4,75E-16	8,80E+30		2,84E+03	4,55E-16	4,60E+30	5,38E+30
5,17E-16	1,15E+31			4,75E-16	1,24E+31			4,55E-16	6,51E+30	7,60E+30
5,17E-16	1,24E+31			4,75E-16	1,34E+31			4,55E-16	7,03E+30	8,21E+30
5,17E-16	1,32E+31			4,75E-16	1,44E+31			4,55E-16	7,51E+30	8,78E+30
5,17E-16	1,40E+31			4,75E-16	1,52E+31			4,55E-16	7,97E+30	9,31E+30
1,91E-16	1,42E+31		1,04E+03	1,67E-16	1,62E+31		1,02E+03	1,63E-16	8,31E+30	9,69E+30
1,91E-16	2,01E+31			1,67E-16	2,30E+31			1,63E-16	1,17E+31	1,37E+31
1,91E-16	2,17E+31			1,67E-16	2,48E+31			1,63E-16	1,27E+31	1,48E+31
1,91E-16	2,32E+31			1,67E-16	2,65E+31			1,63E-16	1,36E+31	1,58E+31
1,91E-16	2,46E+31			1,67E-16	2,81E+31			1,63E-16	1,44E+31	1,68E+31

Energy(MeV)	Beam Energy(MeV/u)	σ(barn) W		L	PWBA	ECPSSR-UA
15	0,118199146	0,011717004			3,40E+01	1,33E-07
30	0,236398292	0,159711954	0,177337558		4,56E+02	2,71E-03
35	0,275798008	0,240430799			7,84E+02	1,08E-02
40	0,315197723	0,34678413	0,338199295		1,24E+03	3,07E-02
45	0,354597439	0,425338709	0,447213087		1,83E+03	7,07E-02
		σ(barn) Au				
15	0,118199146	7,32E-03			1,47E+01	2,37E-08
30	0,236398292	0,058761218			2,13E+02	1,40E-03
35	0,275798008	0,110913726			3,76E+02	6,24E-03
40	0,315197723	0,144959049			6,06E+02	1,93E-02
45	0,354597439	0,174709633			9,13E+02	4,71E-02
		σ(barn) Ta				
15	0,118199146	4,70E-02			4,02E+01	1,82E-07
30	0,236398292	0,114798542	0,21382951		5,30E+02	3,05E-03
35	0,275798008	2,77E-02			9,07E+02	1,18E-02
40	0,315197723	0,273001494	0,439027287		1,43E+03	3,33E-02
45	0,354597439	0,345973867	0,536896397		2,10E+03	7,59E-02
		σ(barn) Ti				
15	0,118199146					
30	0,236398292	0,00938826	0,007596148		2,34E+06	1,44E+04
35	0,275798008	0,021679167			2,74E+06	7,05E+04
40	0,315197723	0,011200432	0,006715737	0,008745	3,10E+06	2,35E+05
45	0,354597439	0,03709518	0,081568685		3,41E+06	6,10E+05
		σ(barn) Cu				
15	0,118199146	7,05E-02			4,29E+05	2,36E-02
30	0,236398292	0,008247021	0,007686342		1,52E+06	2,73E+01
35	0,275798008				1,94E+06	1,68E+02
40	0,315197723	0,017914423	0,015145817		2,36E+06	8,02E+02
45	0,354597439	0,031164473	0,023117864		2,78E+06	3,03E+03
		σ(barn) Nb				
15	0,118199146	1,41E-05			2,04E+04	1,09E-03
30	0,236398292	0,000899334			1,12E+05	2,46E-01
35	0,275798008				1,58E+05	6,82E-01
40	0,315197723	0,008353908			2,10E+05	1,65E+00
45	0,354597439	0,00652143			2,68E+05	3,71E+00
		σ(barn) Ru				
15	0,118199146					
30	0,236398292	0,001772505			6,42E+04	1,59E-01
35	0,275798008	2,86E-03			9,17E+04	4,29E-01
40	0,315197723	0,004955573			1,24E+05	9,94E-01
45	0,354597439	0,009618142			1,60E+05	2,08E+00
		σ(barn) Zn				
15	0,118199146					
30	0,236398292	0,007058612			1,19E+06	1,23E+01
35	0,275798008	3,22E-02			1,54E+06	7,01E+01
40	0,315197723	0,029517897			1,89E+06	3,25E+02
45	0,354597439	0,029015222			2,24E+06	1,23E+03
	NOTE: two different values of cross-section indicated same elements with different compounds					